Zhu *et al. Cell Communication and Signaling* (2024) 22:431
https://doi.org/10.1186/s12964-024-01798-1

Cell Communication
and Signaling

RESEARCH

Open Access

Protein disulfide isomerase plays a crucial role in mediating chemically-induced, glutathione depletion-associated hepatocyte injury in vitro and in vivo

Yan-Yin Zhu[1], Qi Zhang[1], Yi-Chen Jia[1], Ming-Jie Hou[1] and Bao Ting Zhu[1,2*]

Abstract

Recently we have shown that protein disulfide isomerase (PDI or PDIA1) is involved in mediating chemically-induced, glutathione (GSH) depletion-associated ferroptotic cell death through NOS activation (dimerization) and NO accumulation. The present study aims to determine the role of PDI in mediating chemically-induced hepatocyte injury in vitro and in vivo and whether PDI inhibitors can effectively protect against chemically-induced hepatocyte injury. We show that during the development of erastin-induced ferroptotic cell death, accumulation of cellular NO, ROS and lipid-ROS follows a sequential order, *i.e.*, cellular NO accumulation first, followed by accumulation of cellular ROS, and lastly cellular lipid-ROS. Cellular NO, ROS and lipid-ROS each play a crucial role in mediating erastin-induced ferroptosis in cultured hepatocytes. In addition, it is shown that PDI is an important upstream mediator of erastin-induced ferroptosis through PDI-mediated conversion of NOS monomer to its dimer, which then leads to accumulation of cellular NO, ROS and lipid-ROS, and ultimately ferroptotic cell death. Genetic manipulation of PDI expression or pharmacological inhibition of PDI function each can effectively abrogate erastin-induced ferroptosis. Lastly, evidence is presented to show that PDI is also involved in mediating acetaminophen-induced liver injury in vivo using both wild-type C57BL/6J mice and hepatocyte-specific PDI conditional knockout (PDI$^{fl/fl}$ Alb-cre) mice. Together, our work demonstrates that PDI is an important upstream mediator of chemically-induced, GSH depletion-associated hepatocyte ferroptosis, and inhibition of PDI can effectively prevent this injury.

Introduction

Ferroptosis is an iron-dependent, regulated cell death, which is different from apoptosis, necrosis and autophagy and is characterized by the accumulation of lipid peroxides in cells [1]. While the precise biological role of ferroptosis remains to be elucidated, its implications in various human disease conditions have been well established. Ferroptotic cell death is associated with a number of ischemic organ damage (such as ischemic heart disease, ischemic brain injury and renal failure) [1, 2] and chemically-induced, glutathione depletion-associated liver injury [3, 4]. Additionally, there is also evidence suggesting the involvement of ferroptosis in neurodegenerative diseases [5–7].

Biochemically, ferroptosis stems from accumulation of lipid reactive oxygen species (ROS) which exceed cellular antioxidant capacity supported by glutathione (GSH), and from inhibition of glutathione-dependent enzymes, such as glutathione peroxidase GPX4 [8, 9]. Erastin is a small-molecule compound that has been shown to

---

*Correspondence:
Bao Ting Zhu
BTZhu@CUHK.edu.cn
[1] Shenzhen Key Laboratory of Steroid Drug Discovery and Development, School of Medicine, The Chinese University of Hong Kong, 2001 Longxiang Blvd., Longgang District, Shenzhen 518172, Guangdong, China
[2] Shenzhen Bay Laboratory, Shenzhen 518055, China

induce ferroptosis by inhibiting the activity of system Xc^- and resulting in GSH depletion [10]. When the cellular GSH level is reduced, cells become more susceptible to oxidative stress, which, in turn, leads to the occurrence of excessive lipid peroxidation and ultimately ferroptosis. In recent years, erastin has been widely used as a tool compound for studying the mechanism of GSH depletion-associated ferroptotic cell death.

Acetaminophen (APAP) is metabolized in the liver to form a reactive metabolite called *N*-acetyl-*p*-benzoquinone imide (NAPQI). At non-toxic concentrations, NAPQ1 can be effectively detoxified by GSH to form the APAP − GSH conjugates [11]. However, if excessive amount of APAP is taken into the body, NAPQI can readily deplete hepatocyte GSH [11], leading to oxidative stress and lipid peroxidation. The depletion of hepatocyte GSH by APAP is somewhat similar to erastin-induced ferroptosis, which also involves depletion of cellular GSH. In addition, another earlier study reported that APAP can reduce glutathione peroxidase activity by approximately 60% [12], which also contributes to APAP-induced ferroptosis.

Protein disulfide isomerase (PDI or PDIA1) is the prototype of the PDI family proteins, and a ubiquitous dithiol/disulfide oxidoreductase of the thioredoxin superfamily [13–15]. PDI is primarily localized in the endoplasmic reticulum of mammalian cells, although a small fraction of this protein is also found in the nucleus, cytosol, mitochondria, plasma membrane and extracellular space [16, 17]. PDI is involved in protein processing by catalyzing the formation of intra- and inter-molecular disulfide bridges in proteins [18]. PDI in its reduced state can be converted to its oxidized state (*i.e.*, with a disulfide bond formed in its catalytic site), and this step is catalyzed by the ER oxidoreductin 1 (ERO1) [19–21]. Our recent studies have shown that PDI plays an important role in mediating chemically-induced, GSH depletion-associated oxidative cytotoxicity in a number of cell lines [22–24]. Mechanistically, PDI mediates chemically-induced ferroptosis through its ability to catalyze cellular NOS dimerization, which is followed by cellular accumulation of NO, ROS and lipid-ROS, and ultimately ferroptotic cell death [23]. In support of this mechanistic hypothesis, pharmacological inhibition of PDI's enzymatic activity or selective PDI knockdown each can effectively abrogate erastin-induced ferroptosis [22, 23].

The objectives of our present study are two-fold: one is to examine the role of PDI in mediating chemically-induced hepatocyte injury in vitro and in vivo, and the other one is to determine whether PDI inhibitors (such as cystamine) can effectively protect against chemically-induced hepatocyte injury in vitro and in vivo. To achieve these experimental goals, erastin was used to induce ferroptotic cell death in cultured BRL-3A normal rat hepatocytes as an *in-vitro* model for chemically-induced, GSH depletion-associated ferroptosis. The main reasons for the selection of BRL-3A rat hepatocytes as an *in-vitro* model in this study are: ***i***. The BRL-3A rat hepatocytes are normal rat liver cells (*i.e.*, they are non-cancer cells). ***ii***. This cell line is highly sensitive to erastin-induced oxidative ferroptosis in vitro, and the cell death can be readily rescued by classical ferroptosis inhibitors such as ferrostatin-1 (shown later). On the other hand, APAP was used in the wild-type C57BL/6J mice and in hepatocyte-specific PDI conditional knockout ($PDI^{fl/fl}$ Alb-cre) mice as *in-vivo* models to induce GSH depletion-associated hepatocyte injury. Experimental evidence was provided to show that PDI plays an important role in mediating chemically-induced hepatocyte forroptosis both in vitro and in vivo. Also, we showed that PDI inhibitor(s) can be used to effectively protect hepatocytes against chemically-induced oxidative ferroptosis both in vitro and in vivo.

Materials and methods

Chemicals and reagents

Erastin (#S7242) was obtained from Selleck (Houston, Texas, USA); *N*-acetyl-*L*-cysteine (NAC, #A8199), (±)-6-hydroxy-2,5,7,8-tetramethylchromane-2-carboxylic acid (Trolox, #238813), cystamine dihydrochloride (cystamine, #C121509) and acetaminophen (APAP, #A7085) from Sigma-Aldrich (Saint Louis, Missouri, USA); thiazolyl blue tetrazolium bromide (MTT, #T818538) from MACKLIN (Shanghai, China); carboxy-PTIO (cPTIO, #S1547), diaminofluorescein-FM diacetate (DAF-FM-DA, #S0019) and 2',7'-dichlorodihydrofluorescein diacetate (DCFH-DA, #S0033S) from Beyotime Biotechnology (Shanghai, China); BODIPY™-581/591-C11 (#D3861) from ThermoFisher Scientific (Waltham, Massachusetts, USA); EN460 (#M07515) from BioLab (Beijing, China); and ferrostatin-1 (Fer-1, #HY-100579) from MedChemExpress (NJ, USA). The anti-iNOS antibody (#ab15323) was obtained from Abcam (Cambridge, UK), the anti-PDI antibody (#3501S) from Cell Signaling Technology (Boston, Massachusetts, USA), the primary anti-CYP2E1 antibody (#A22629) from ABclonal (Wuhan, China), the anti-β-actin antibody (#GB15001) and the HRP conjugated goat anti-mouse IgG (H + L) (#gb23301) from ServiceBio (Wuhan, China), and the rabbit anti-PDI antibody (#bs-0295G-HRP) from Bioss (Beijing, China). Calcein-AM/PI Cell Viability/Cytotoxicity Assay Kit (#C2015M) was purchased from Beyotime Biotechnology (Shanghai, China), Glutamic Pyruvic Transaminase (GPT) Kit (#C009-2–1) and Glutamic Oxalacetic Transaminase (GOT) Kit (#C010-2–1) from Nanjing Jiancheng Bioengineering Institute (Nanjing, China), and

Malondialdehyde (MDA) Content Assay Kit (#BC0025) from SolarBio (Beijing, China). The siRNAs for rat PDI were obtained from Sangon Biotech (Shanghai, China). The siRNAs sequences for rat PDI are CCAAGUACC AGCUGGACAATT (sense) and UUGUCCAGCUGG UACUUGGTT (antisense) for siPDI-1; GCAAGAUCC UGUUCAUCUUTT (sense) and AAGAUGAACAGG AUCUUGCTT (antisense) for siPDI-2; GCAGCCAGU GAAAGUGCUATT (sense) and UAGCACUUUCAC UGGCUGCTT (antisense) for siPDI-3. A mixture of the three pairs of siRNAs was used in the transfection experiments. Most of the other chemicals used in this study, unless specified otherwise, were obtained from Sigma-Aldrich (Saint Louis, Missouri, USA).

Cell culture conditions and measurement of cell viability

The BRL-3A normal rat liver cells were obtained from the Cell Bank of the Chinese Academy of Sciences (Shanghai, China), cultured in DMEM supplemented with 10% (*v*/*v*) fetal bovine serum and 1% penicillin and streptomycin at 37 °C under 5% CO_2. Cells were sub-cultured when they reached approximately 80% confluence.

The MTT reduction assay was used to determine the gross cell viability. The BRL-3A cells were seeded in 96-well plates at a density of 2,000 cells/well 12 h prior to receiving different experimental treatments. To test the modulating effect of a compound on erastin-induced ferroptosis, the cells were treated with erastin ± the compound for 24 h. Then, MTT at a final concentration of 0.5 mg/mL was added to each well, and incubated for 2.5 h at 37 °C under 5% CO_2. After incubation, the MTT-containing medium was removed and 100 μL DMSO was added to each well to dissolve the MTT formazan. Absorbance of the MTT formazan was measured with a microplate reader (BioTek, Winooski, VT, USA) at 560 nm.

Measurement of cellular NO, ROS and lipid-ROS levels

The cellular levels of NO, ROS and lipid-ROS were jointly determined using analytical flow cytometry and fluorescence/confocal microscopy. The BRL-3A cells were seeded in 24-well plates at a density of 4×10^4 cells/well 12 h before treatment, and then the cells were treated with erastin ± various modulating compounds for 8 h. The cells were washed with HBSS twice, and the cellular levels of NO, ROS and lipid-ROS were detected after addition of the cell-permeant fluorescent probes DAF-FM-DA (10 μM, for detection of NO), DCFH-DA (5 μM, for detection of ROS) or BODIPY-581/591-C11 (5 μM, for detection of lipid-ROS) dissolved in 200 μL phenol red- and serum-free DMEM. The cells were incubated at 37 °C for an additional 30 and then washed twice with HBSS. The fluorescence intensity reflecting the cellular accumulation NO, ROS and lipid-ROS was detected by MoFlo-XDP cell sorter (Beckman Coulter, Indianapolis, IN, USA) and analyzed by the FlowJo software (FlowJo, LLC, Ashland, OR, USA). The fluorescence microscope images of cellular NO and ROS were taken by a Nikon Eclipse Ti-U inverted microscope (Nikon, Tokyo, Japan) and analyzed with the NIS-Elements software (Nikon); the fluorescence microscope images of cellular lipid-ROS were taken using a confocal laser scanning microscope (LSM 900; Carl Zeiss, Oberkochen, Germany) and analyzed with the Zen software (Carl Zeiss).

Purification of PDI

The cDNA for human PDI protein was cloned into the pET-28a vector, and the expressed PDI protein was purified using the Ni–NTA agarose (QIAGEN) and separated using the ÄKTA FPLC system as described previously [25–28]. The purified PDI protein was analyzed using Western blotting and its protein concentration was determined by Bio-Rad Protein Assay Kit using BSA as standard.

qRT-PCR analysis

For qRT-PCR analysis, fresh cells or tissues were first lysed with the TRIzolTM reagent (#15596018; Invitrogen, Waltham, Massachusetts, USA), extracted with chloroform, precipitated with isopropyl alcohol, and washed with 75% ethanol to dissolve RNAs in the RNase-free sterile water. The primer sequences used in this study are listed in Table 1, and synthesized by Sangon Biotech (Shanghai, China). For reverse transcription and q-PCR, the Reverse Transcription Kit (#RR047) and TB Green® (#RR820) from TAKARA (Japan) were used.

Table 1 Primer sequences used in the qRT-PCR analysis

Target gene	Forward primer (5′-3′)	Reverse primer (5′-3′)
GPX4 (mice)	ATAAGAACGGCTGCGTGGTGAAG	TAGAGATAGCACGGCAGGTCCTTC
ERO1α (mice)	TGCCGTCAAACCCTGCCATTC	AGTCGCTCAGCTTGCTCACATTC
PDI (mice)	GCTGTTCCTGCCCAAGAGTGTATC	CTGGTTATCAGTGTGGTCGCTATCG
β-actin (mice)	AAATCGTGCGTGACATCAAAGA	GCCATCTCCTGCTCGAAGTC

Immunoblot analysis

After treatment of BRL-3A cells with erastin for different lengths of time as indicated, the cells were collected by trypsinization and centrifugation, and then lysed in a RIPA buffer containing 1% protease inhibitor cocktail on ice for 30 min. Protein concentrations were determined using the BCA Assay Kit (ThermoFisher). For total iNOS analysis (including both monomeric and dimeric forms of iNOS), samples were heated at 100 °C for 10 min with a reducing buffer before loaded onto the gel. To analyze the monomeric and dimeric forms of iNOS, samples were prepared with a non-reducing buffer and were not heated, and the temperature of the gel was maintained below 15 °C during electrophoresis. Proteins were then separated using 8% agarose gel (for total iNOS) or 6% agarose gel (for monomeric and dimeric iNOS), and then transferred to PVDF membranes. After the membranes were incubated for 1 h in 5% skim milk at room temperature, they were incubated with the primary antibody overnight. Afterwards, the membranes were washed three times with TBST at room temperature (10 min each time). The membranes were then incubated with the secondary antibody for 1 h at room temperature and washed with TBST three times before visualization. Desired protein bands were visualized using the Tanon-5200 Chemiluminescence Imaging System (Shanghai, China).

Animal experiments

All procedures involving the use of live animals described in this study were approved by the Institutional Animal Care and Use Committee (IACUC) of The Chinese University of Hong Kong (Shenzhen), and the guidelines for the humane care of animals set forth by the U.S. National Institutes of Health were followed.

The hepatocyte-specific PDI$^{fl/fl}$ mice were prepared. The C57BL/6J-P4hbem1 Smoc (P4hb-Flox) mice were generated using CRISPR/Cas9-based technology. Specifically, Cas9 mRNA and gRNA were obtained via *in-vitro* transcription. An *in-fusion* cloning method was employed to construct a homologous recombination donor vector, which comprised of a 3.0-kb 5'-homologous arm, a 3.1-kb Flox region, and a 3.0-kb 3'-homologous arm. Cas9 mRNA, gRNA, and the donor vector were microinjected into fertilized eggs of the C57BL/6J mice to generate the F0 (chimera) generation. The positive F0 mice were identified through PCR amplification and sequencing. Subsequently, the positive F1 P4hb-Flox mice were obtained by mating these mice with the C57BL/6J mice. The genotype of the mice was confirmed by sequencing the PCR fragments, with the following PCR primers: TCGAAGGTTTCCCAGTGAGC for Flox-F1 (P4hb-Flox-F1), and AGATCCACCAGCCTCTACCC for Flox-R1 (P4hb-Flox-R1). All mice were maintained in a pathogen-free animal facility at The Chinese University of Hong Kong (Shenzhen).

The wild-type C57BL/6J male mice (9–11 weeks old) were purchased from Charles River (China) and the homozygous Alb-Cre mice from Cyagen (Suzhou, China). These mice expressed the Cre recombinase gene under the control of the albumin promoter, conferring hepatocyte-specific Cre-mediated recombination. The PDI-floxed mice were crossed with the Alb-Cre mice to generate hepatocyte-specific PDI conditional knockout mice. The resulting heterozygous offspring mice (PDI$^{fl/+}$, Alb-cre) were self-bred to produce homozygous offspring (PDI$^{fl/fl}$, Alb-cre). Genotyping of the offspring mice was performed to confirm the presence of PDI-floxed and Alb-Cre alleles. The tail DNA was extracted from the mice, and PCR amplification was carried out using primers specific for PDI-floxed and Alb-Cre alleles. The primers for Alb-Cre PCR were GAAGCAGAAGCTTAGGAA GATGG for Alb-Cre-F (F1) and TTGGCCCCTTACCAT AACTG for Alb-Cre-R (R1); primers for the wild-type PCR were TGCAAACATCACATGCACAC for WT-F (F2) and TTGGCCCCTTACCATAACTG for Alb-Cre-R (R1).

For APAP-induced hepatocyte injury, the mice were randomly divided into different experimental groups (with 5 animals per group) with comparable average body

(See figure on next page.)

Fig. 1 Dose- and time-dependent induction of cell death and cellular NO, ROS/lipid-ROS accumulation by erastin in BRL-3A rat hepatocytes. **A** Dose-dependent induction by erastin of ferroptotic cell death. Cells were seeded in 96-well plates at 2000 cells/well, and 12 h later, they were treated with different concentrations of erastin for an additional 24 h. Cell viability was determined by MTT assay ($n=5$). **B**, **C**, **D**, **E** Dose- and time-dependent induction by erastin of cellular NO accumulation (**B**, **D** for fluorescence microscopy, scale bar = 25 μm; **C**, **E** for flow cytometry). Cells were treated with increasing concentrations of erastin for 8 h (**B**, **C**) or treated with 2.5 μM erastin for different durations (**D**, **E**). Quantitative values for **B**–**E** are shown in Supplementary Fig. S2A–S2D. **F**, **G**, **H**, **I** Dose- and time-dependent induction by erastin of cellular ROS accumulation (**F**, **H** for fluorescence microscopy, scale bar = 25 μm; **G**, **I** for flow cytometry). Cells were treated with increasing concentrations of erastin for 8 h (**F**, **G**) or treated with 2.5 μM erastin for different durations (**H**, **I**). Quantitative values for **F**–**I** are shown in Supplementary Fig. S2E–S2H. **J**, **K**, **L** Dose- and time-dependent induction by erastin of cellular lipid-ROS accumulation (**J**, **K** for flow cytometry; **L** for confocal microscopy, scale bar = 5 μm). In **L**, the oxidized dye (in green) reflects lipid-ROS. Quantitative values for **J**–**L** are shown in Supplementary Fig. S2I–S2K. Each value represents the mean ± S.D. (** $P<0.01$; n.s. not significant)

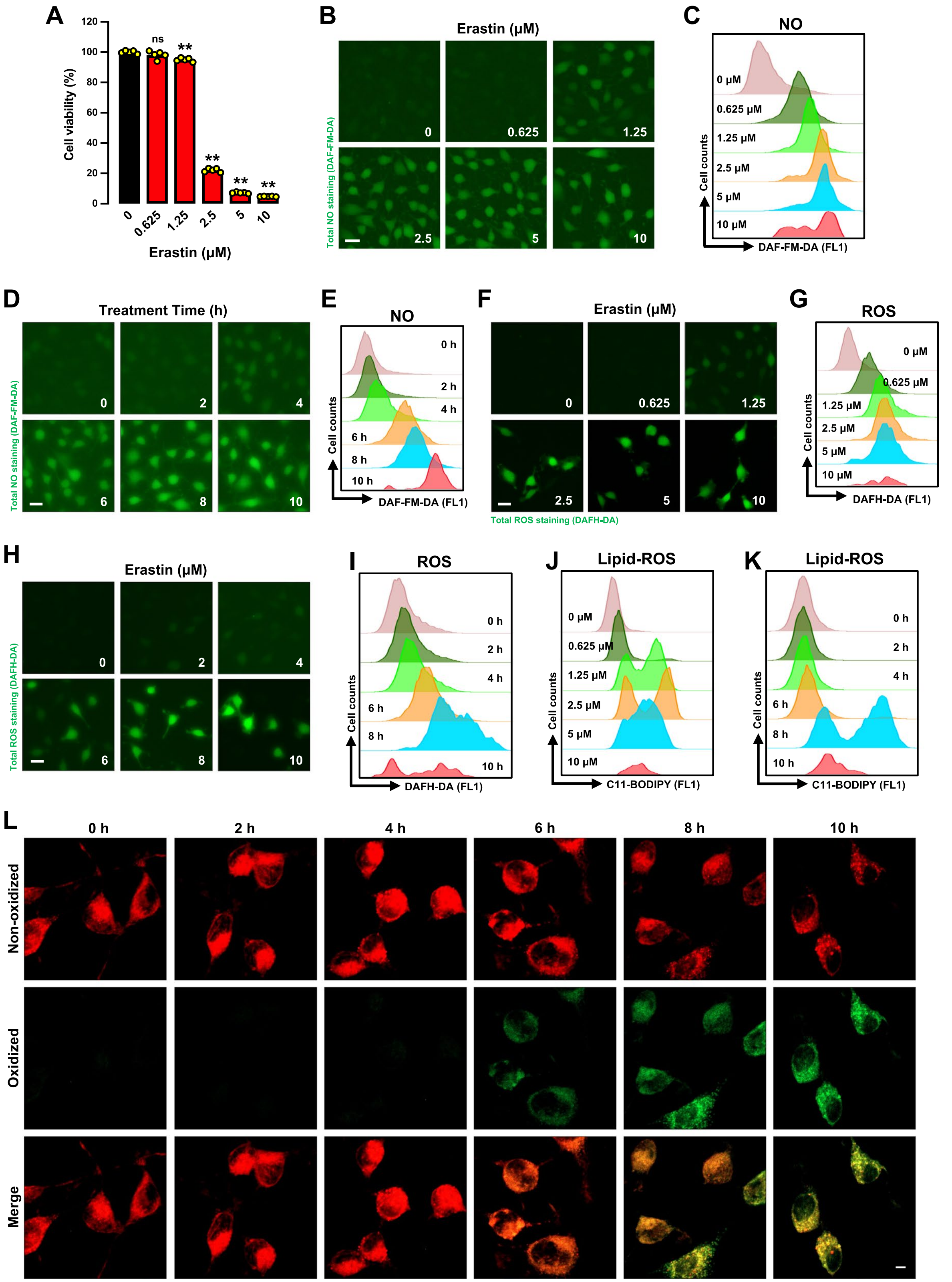

Fig. 1 (See legend on previous page.)

weights. APAP was given to mice by gastric intubation at a dose of 300 mg/kg, and cystamine was injected intraperitoneally (*i.p.*) at a dose of 40 mg/kg. The plasma levels of GPT, GOT and MDA were determined using the GPT, GOT and MDA kits according to manufacturers' instructions.

Histological and immunohistochemical staining of tissue slides

Fresh mouse liver tissues were placed in 10% formalin solution and stored for at least three days before dehydration. The tissues were sectioned into 4-μm thickness after completion of dehydration and paraffin embedding. For H/E staining, the Hematoxylin and Eosin Staining Kit (H/E, #BL700B, BioSharp, Anhui, China) was used. For IHC staining of CYP2E1 and PDI proteins, the slides were incubated with the primary anti-CYP2E1 antibody (#A22629, 1:800; ABclonal, Wuhan, China) or anti-PDI antibody (#3501S, 1:1250; Cell Signaling Technology, Boston, Massachusetts, USA) at 4 °C overnight, and then further incubated with the secondary antibody (rabbit polymer detect system; #PV-6001; ZSGB-BIO, Beijing, China) for 1 h. They were then stained with the DAB Kit (#ZLI-9017, ZSGB-BIO, Beijing, China), and images were captured at desired magnifications with an upright microscope.

Statistical analysis

Most of the experiments and quantitative data described in this study were repeated multiple times which showed a highly similar trend. The data were presented as the mean ± S.D. from multiple replicate measurements (usually from one representative experiment). Statistical analysis was conducted using one-way or two-way ANOVA, followed by Dunnett's *post-hoc* tests for multiple comparisons as needed (GraphPad Prism 8, GraphPad Software, La Jolla, CA). Statistical significance was denoted by $P < 0.05$ (* or $^{\#}$) and $P < 0.01$ (** or $^{\#\#}$) for significant and very significant differences, respectively. In most cases, * and ** denote the comparison for statistical significance between the control group (cells treated with vehicle only) and the cells treated with erastin, whereas $^{\#}$ and $^{\#\#}$ denote the comparison between the cells treated with erastin and the cells jointly treated with erastin and another compound. For Western blot quantification, one representative data is shown.

Results

Changes in cellular NO, ROS and lipid-ROS levels in erastin-treated rat hepatocytes

After the BRL-3A rat hepatocytes were treated with erastin at different concentrations for 24 h, the cell viability (based on MTT assay) was found to be decreased in a concentration-dependent manner (Fig. 1A, Supplementary Fig. S1). It is of note that erastin had a rather steep dose–response curve at concentrations between 1.25 – 2.5 μM. The same experiments were repeated multiple times, and a similar trend was observed (Supplementary Fig. S1). The estimated IC_{50} value of erastin in BRL-3A rat hepatocytes ranged between 1.25 – 2.5 μM. We chose 2.5 μM erastin (a concentration that reduces the cell viability by approximately 80%; see Fig. 1A) for many subsequent experiments, including those that were designed to study the protective effect of different chemicals.

In our recent studies [22–24], we found that during the induction of GSH depletion-associated ferroptotic cell death, there was a time-dependent NO accumulation occurring first, followed by ROS/lipid-ROS accumulation. Next, we determined the effect of erastin on cellular NO, ROS and lipid-ROS accumulation in BRL-3A cells. Based on fluorescence microscopic and flow cytometry

(See figure on next page.)

Fig. 2 Change in cellular iNOS protein and NO levels during erastin-induced ferroptosis in BRL-3A rat hepatocytes. **A**, **B**, **C** Erastin-induced increase in iNOS protein (**A**, **B**) and its monomer and dimer forms (**C**). Cells were treated with erastin with different concentrations of erastin as indicated for 8 h (**A**) or treated with 2.5 μM erastin for different durations (**B**, **C**), and then determined for iNOS total protein levels (**A, B**) or its monomer or dimer forms (**C**). **D** Effect of SNP on erastin-induced ferroptotic cell death (MTT assay, $n = 4$). Cells were treated with 200 μM SNP ± different concentrations of erastin for 24 h. **E**, **F** Effect of SNP on erastin-induced cellular ROS and lipid-ROS accumulation (**E** for fluorescence microscopy, scale bar = 25 μm; **F** for confocal microscopy, scale bar = 5 μm). Levels of cellular ROS and lipid-ROS were determined after treatment with erastin (2.5 μM) ± SNP (200 μM) for 8 h. Quantitative values for **E** and **F** are shown in Supplementary Fig. S3A and S3B. **G**, **H** Protective effect of cPTIO against erastin-induced ferroptotic cell death (**G** for MTT assay; **H** for flow cytometry of Calcein-AM/PI staining). In **G**, cells were jointly treated with different concentrations of cPTIO ± 2.5 μM erastin for 24 h ($n = 4$); in **H**, cells were first treated with erastin (2.5 μM) ± cPTIO (100 μM) for 8 h, and then stained with Calcein-AM (200 nM) and PI (50 μg/mL) for 20 min. **I**, **J**, **K**, **L** Protective effect of cPTIO against erastin-induced accumulation of cellular NO and ROS (**I**, **K** for fluorescence microscopy, scale bar = 25 μm; **J**, **L** for flow cytometry, $n = 3$). Cells were treated with 2.5 μM erastin ± 100 μM cPTIO for 8 h and stained with DAF-FM-DA for NO (**I**, **J**) or DCFH-DA for ROS (**K**, **L**). Quantitative values for **I** and **K** are shown in Supplementary Fig. S3C and S3D. **M**, **N** Protective effect of cPTIO against erastin-induced accumulation of lipid-ROS (**M** for flow cytometry, $n = 3$; **N** for confocal microscopy, scale bar = 5 μm). Cells were treated with 2.5 μM erastin ± 100 μM cPTIO for 8 h and then stained with BODIPY™-581/591-C11 for lipid-ROS. **O** Effect of cPTIO on erastin-induced change in total iNOS and PDI protein levels (Western blotting). The drug treatments were the same as in **I, K**. Each value represents the mean ± S.D. ($^{\#}P < 0.05$; ** or $^{\#\#}P < 0.01$)

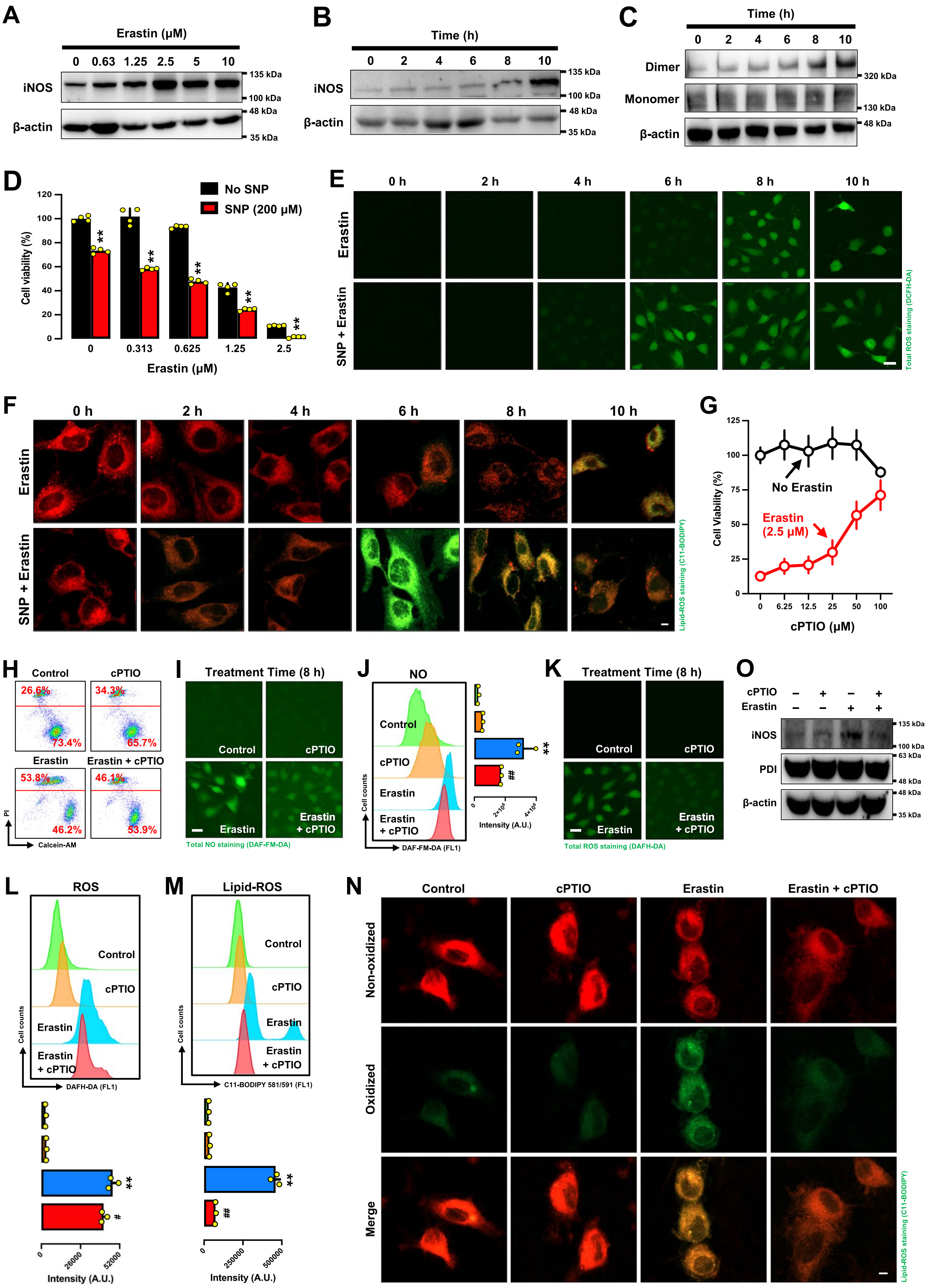

Fig. 2 (See legend on previous page.)

analysis of DAF-FM-DA-stained cells, erastin treatment stimulated NO accumulation in a concentration-dependent manner, and a near maximal accumulation of NO was observed when 5 μM erastin was present (Fig. 1B, C). Furthermore, the increase in cellular NO levels was also time-dependent, which became clearly detectable at 4 h following erastin exposure and then continued to increase at 8 and 10 h (Fig. 1D, E).

Similarly, the levels of cellular ROS (stained with DCFH-DA) were also increased by erastin treatment in a concentration-dependent manner (Fig. 1F, G). In addition, the cellular ROS level also gradually increased in a time-dependent manner following exposure to 2.5 μM erastin: the signal became detectable at approximately 6 h after erastin treatment, and near maximal accumulation was observed at approximately 8 h after erastin exposure (Fig. 1H, I). The initial small increase in cellular ROS levels starts approximately 2 h behind the NO accumulation, which is in agreement with our earlier observations [22–24].

Accumulation of cellular lipid peroxides is a hallmark in chemically-induced ferroptotic cell death [29]. The change in lipid-ROS levels was determined in cells treated with different concentrations of erastin or with 2.5 μM erastin for different durations. Erastin-treated cells were stained with C11-BODIPY-581/591 (FL1), and then subjected to analytical flow cytometry or confocal microscopy. Cellular lipid-ROS accumulation was increased significantly after treatment with 0.625 μM erastin, reaching a peak at 2.5 μM erastin (Fig. 1J). Time-dependency analysis showed that lipid-ROS became detectable at 6 h and peaked at 8 h in cells treated with 2.5 μM erastin (Fig. 1K, L).

In summary, it is evident that treatment of BRL-3A rat hepatocytes with erastin induces the accumulation of cellular NO, ROS and lipid-ROS in a time-dependent manner, in an apparent sequential order of NO accumulation occurring first, followed by ROS/lipid-ROS.

Role of iNOS and NO accumulation in erastin-induced ferroptosis in rat hepatocytes

Induction of iNOS in erastin-treated hepatocytes

In addition to measuring the change in cellular NO levels in erastin-treated cells, the change in cellular iNOS which catalyzes the formation of NO was also determined. Erastin treatment caused a concentration-dependent increase in total iNOS protein level (Western blotting), and the total iNOS protein levels peaked in cells treated with erastin at concentrations ≥ 2.5 μM (Fig. 2A). In addition, erastin treatment also caused a time-dependent increase in iNOS total protein level, which peaked at approximately 10 h after erastin treatment (Fig. 2B). Using the non-reducing gel electrophoresis coupled with Western blotting, it was observed that the level of iNOS dimer protein was also increased in a time-dependent manner (Fig. 2C).

Role of NO in erastin-induced cell death

To probe the role of NO in erastin-induced cell death in rat hepatocytes, we examined the effect of sodium nitroprusside (SNP), an NO donor [30], on cellular ROS and lipid-ROS accumulation. We found that the presence of 200 μM SNP enhanced erastin-induced cytotoxicity (Fig. 2D), and also increased cellular accumulation of cellular ROS and lipid-ROS 2 h earlier than the presence of erastin alone (Fig. 2E, F).

Carboxy-PTIO (cPTIO), a known NO scavenger [31], was used to probe the role of cellular NO in erastin-induced cell death. We found that cPTIO at 100 μM provided a significant protection against erastin-induced cytotoxicity (Fig. 2G). This strong cytoprotective effect of cPTIO was confirmed by analyzing changes in cellular gross morphology (Supplementary Fig. S7) or Calcein-AM/PI double staining of live and dead cells (Fig. 2H). We also determined the effect of cPTIO on cellular NO, ROS and lipid-ROS levels by jointly using fluorescence microscopy and analytical flow cytometry. At 8 h following erastin exposure, the cellular NO level was increased, but joint treatment with cPTIO reduced NO accumulation (Fig. 2I, J). As expected, a similar increase in cellular ROS levels was observed in erastin-treated cells, and joint treatment with cPTIO effectively abrogated

(See figure on next page.)

Fig. 3 Protective effect of SMT against erastin-induced ferroptosis in BRL-3A rat hepatocytes. **A** Protective effect of SMT against erastin-induced loss of cell viability (MTT assay). The cells were treated with different concentrations of SMT ± erastin (2.5 μM) for 24 h (mean ± S.D., $n = 4$). **B** Protective effect of SMT against erastin-induced cell death (flow cytometry). Cells were first treated erastin (2.5 μM) ± SMT (400 μM) for 8 h, and then stained with Calcein-AM (200 nM) and PI (50 μg/mL) for an additional 20 min.**C**, **D**, **E**, **F** Protective effect of SMT against erastin-induced accumulation of cellular NO and ROS (**C**, **E** for fluorescence microscopy, scale bar = 25 μm; **D**, **F** for flow cytometry, $n = 3$). Quantitative values for **C** and **E** are shown in Supplementary Fig. S4A and S4B. **G**, **H** Protective effect of SMT against erastin-induced accumulation of cellular lipid-ROS (**G** for confocal microscopy, scale bar = 5 μm; **H** for flow cytometry, $n = 3$). **I** Effect of SMT on erastin-induced change in total iNOS and PDI protein levels (Western blotting). The drug treatment condition was the same as in **B**. Each value represents the mean ± S.D. (** or.$^{\#\#}P < 0.01$)

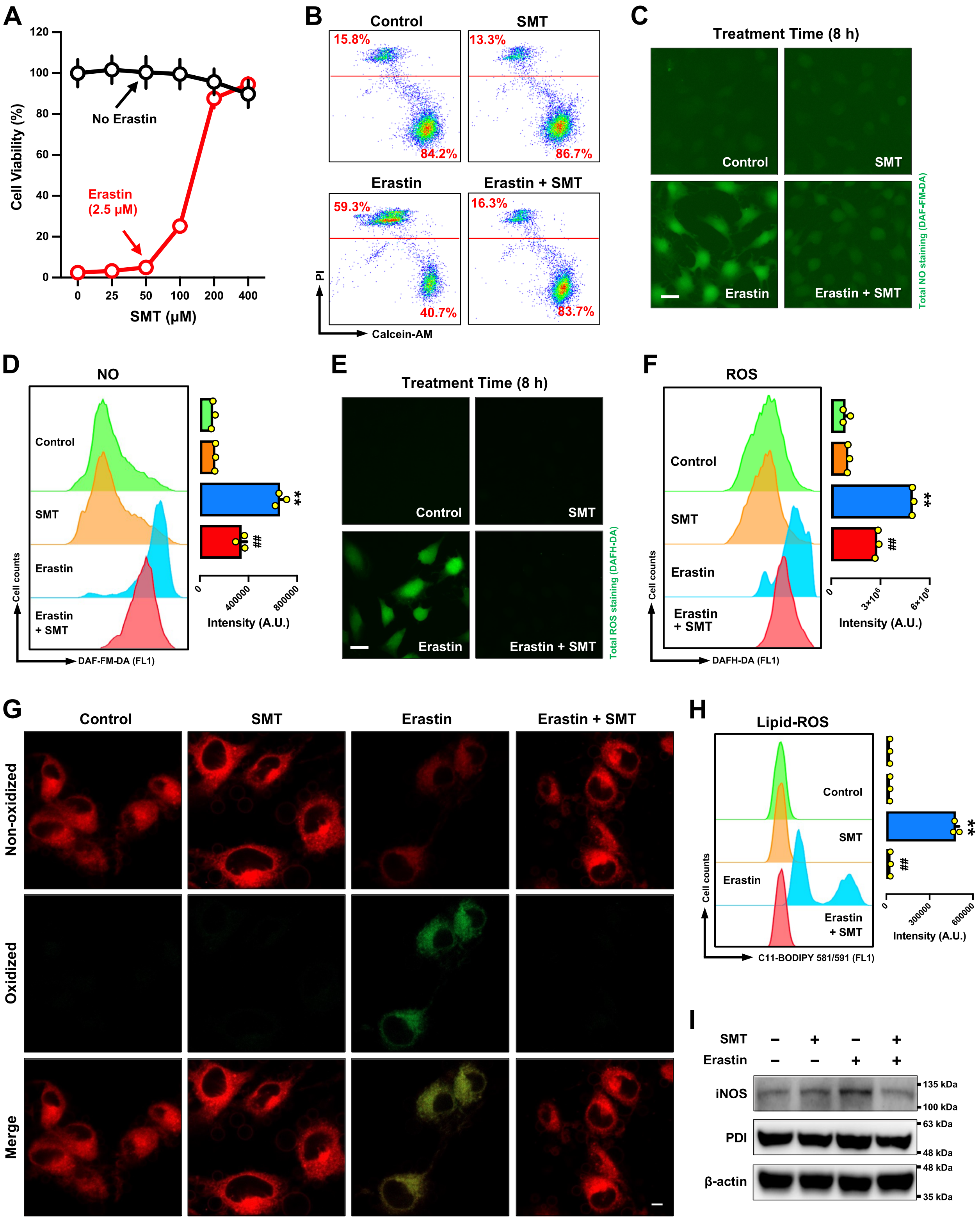

Fig. 3 (See legend on previous page.)

erastin-induced ROS accumulation (Fig. 2K, L). In addition, confocal microscopic analysis showed that joint treatment of cells with cPTIO abrogated erastin-induced lipid-ROS accumulation (Fig. 2M, N).

The change in iNOS and PDI protein levels in cells treated with erastin ± cPTIO was also determined. After 8-h treatment with erastin with or without cPTIO, the cells were collected and lysed for Western blotting. The results showed that erastin significantly increased total iNOS protein level, while joint treatment with cPTIO abrogated erastin-induced increase in total iNOS protein level. In comparison, the PDI protein levels were not significantly different in different treatment groups (Fig. 2O).

S-Methylisothiourea sulfate (SMT) is an inhibitor of iNOS [32]. Based on the MTT assay, SMT exerted a strong protective effect against erastin-induced ferroptosis in BRL-3A hepatocytes, and the protective effect was most pronounced at 400 μM (Fig. 3A, B, Supplementary Fig. S8). Next, we examined the effect of SMT on erastin-induced accumulation of cellular NO, ROS and lipid-ROS. Fluorescence microscopy and flow cytometry results both showed that SMT effectively abrogated erastin-induced accumulation of NO, ROS and lipid-ROS (Fig. 3C–H). Western blotting results showed that joint treatment with SMT abrogated erastin-induced increase in total iNOS protein level, while the PDI protein level was not markedly altered (Fig. 3I).

Role of ROS and lipid-ROS accumulation in erastin-induced ferroptosis in rat hepatocytes

Trolox

We investigated the effect of (±)-6-hydroxy-2,5,7,8-tetramethylchromane-2-carboxylic acid (Trolox), an ROS scavenger [33], on erastin-induced ferroptosis. Based on MTT assay and analysis of cellular gross morphology, Trolox exerted a quite strong protection against erastin-induced cell death in a concentration-dependent manner, and approximately 80% protection was observed when Trolox was present at 100 μM (Fig. 4A, Supplementary Fig. S9). The cytoprotective effect of Trolox against erastin-induced cell death was confirmed using the Calcein-AM/PI assay (Fig. 4B).

Next, we determined the change in cellular NO, ROS and lipid-ROS accumulation in cells treated erastin ± Trolox. Trolox exerted a rather modest protection against erastin-induced NO accumulation (Fig. 4C, D). Similarly, Trolox also modestly abrogated erastin-induced ROS accumulation (Fig. 4E, F). Confocal microscopy showed that Trolox exerted a stronger reduction of erastin-induced lipid-ROS accumulation (Fig. 4G), and this observation was confirmed by analytical flow cytometry (Fig. 4H). These results clearly indicate that Trolox (which is a highly lipophilic compound) has a preferential scavenging activity for lipid-ROS, and this effect is also consistent with its rather strong protective effect against earstin-induced cytotoxicity.

NAC

N-Acetyl-*L*-cysteine (NAC) is a powerful antioxidant and ROS scavenger [34, 35]. Joint treatment of cells with NAC strongly protected against erastin-induced cell death, and a maximum protection (nearly 100%) was observed at 400 μM NAC (Fig. 4I, J, Supplementary Fig. S10). NAC abrogated erastin-induced accumulation of cellular NO (Fig. 4K, L), ROS (Fig. 4M, N) and lipid-ROS (Fig. 4O, P). It is of note that joint treatment of cells with NAC also effectively abrogated erastin-induced increase in total iNOS protein level (Fig. 4Q); this effect on erastin-induced iNOS protein increase contributes to its partial abrogation of erastin-induced increase in cellular NO levels.

(See figure on next page.)

Fig. 4 Protective effect of Trolox and NAC against erastin-induced ferroptosis in BRL-3A rat hepatocytes. **A**, **B** Protective effect of Trolox against erastin-induced cell death (**A** for MTT assay; **B** for flow cytometry). In **A**, cells were treated with increasing concentrations of Trolox ± erastin (2.5 μM) for 24 h (*n* = 4); in **B**, cells were first treated with erastin (2.5 μM) ± Trolox (100 μM) for 8 h, and then stained with Calcein-AM (200 nM) and PI (50 μg/mL) for an additional 20 min. **C, D, E, F.** Protective effect of Trolox against erastin-induced accumulation of cellular NO and ROS (**C, E** for fluorescence microscopy, scale bar = 25 μm; **D**, **F** for flow cytometry, *n* = 3). Quantitative values for C and E are shown in Supplementary Fig. S5A and S5B. **G**, **H** Protective effect of Trolox against erastin-induced accumulation of cellular lipid-ROS (**G** for confocal microscopy, scale bar = 5 μm; **H** for flow cytometry, *n* = 3). The drug treatment condition was the same as in **B**. **I**, **J** Protective effect of NAC against erastin-induced ferroptotic cell death (**I** for MTT assay; **J** for flow cytometry). In **I**, cells were treated with increasing concentrations of NAC ± erastin (2.5 μM) for 24 h (*n* = 4); in **J**, cells were first treated with erastin (2.5 μM) ± NAC (400 μM) for 8 h, and then stained with Calcein-AM (200 nM) and PI (50 μg/mL) for an additional 20 min. **K**, **L**, **M**, **N** Protective effect of NAC against erastin-induced accumulation of NO and ROS (**K**, **M** for fluorescence microscopy, scale bar = 25 μm; **L**, **N** for flow cytometry, *n* = 3). Quantitative values for **K** and **M** are shown in Supplementary Fig. S5C and S5D. **O**, **P** Protective effect of NAC against erastin-induced accumulation of lipid-ROS (**O** for confocal microscopy, scale bar = 5 μm; **P** for flow cytometry, *n* = 3). **Q** Effect of NAC on erastin-induced change in total iNOS and PDI protein levels (Western blotting). The drug treatment condition was the same as in **J**. Each value represents the mean ± S.D. (* or $^{\#}P < 0.05$; ** or.$^{\#\#}P < 0.01$)

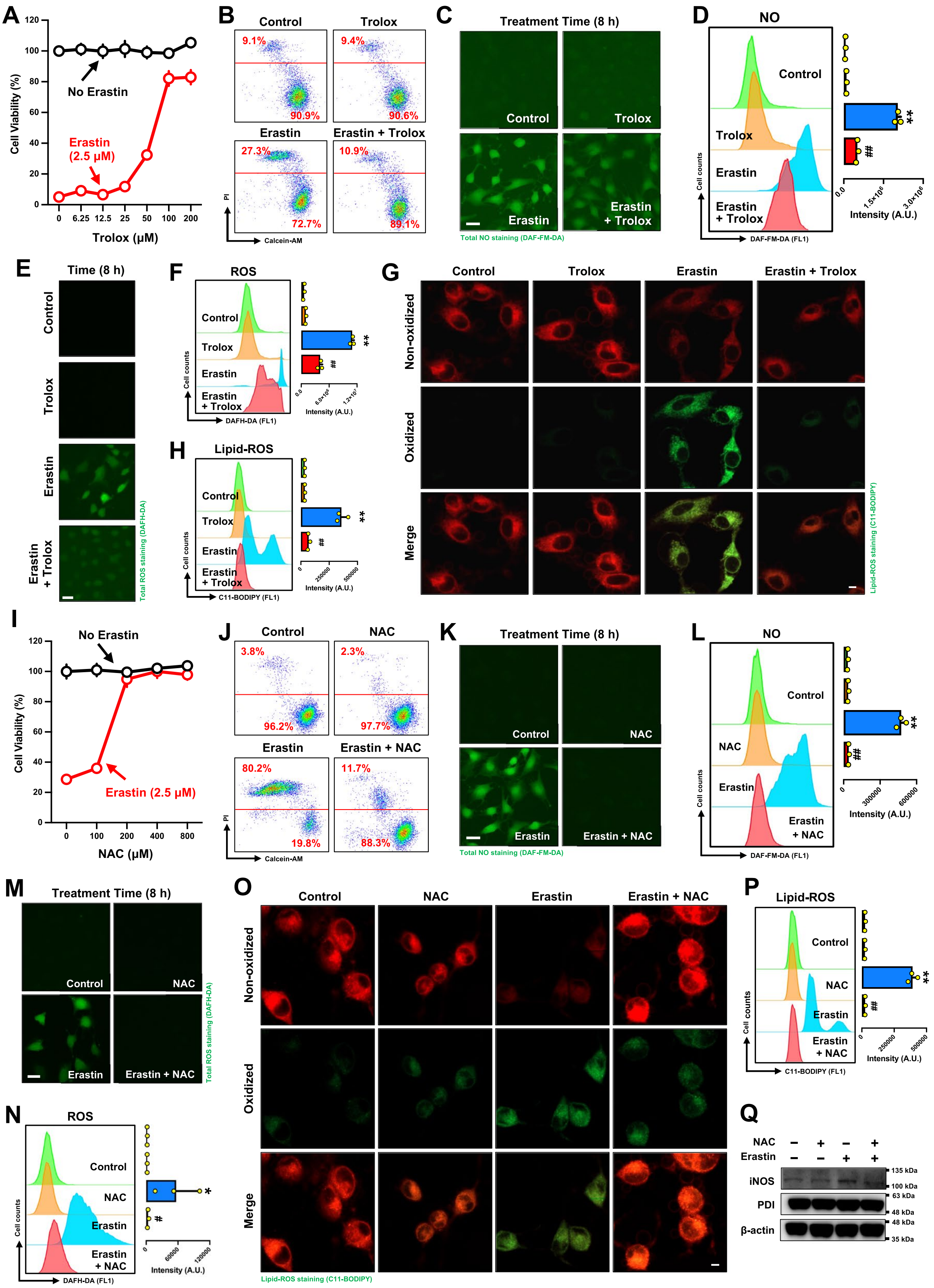

Fig. 4 (See legend on previous page.)

Fer-1

Ferrostatin-1 (Fer-1) is a lipid-ROS scavenger and also a potent inhibitor of ferroptosis [36]. We found that Fer-1 (at 100 nM) strongly protected against erastin-induced ferroptosis, with nearly 100% protection (Fig. 5A, Supplementary Fig. S11). As expected, Fer-1 strongly abrogated erastin-induced accumulation of lipid-ROS (Fig. 5B, C), while it partially reduced the accumulation of ROS (Fig. 5F, G). Notably, erastin-induced accumulation of NO was also partially reduced by Fer-1 (Fig. 5D, E). Fer-1 also significantly reduced erastin-induced increase in total iNOS protein level (Fig. 5H), which may also contribute to the observed reduction in cellular NO accumulation.

Role of PDI in mediating erastin-induced ferroptosis in rat hepatocytes

Effect of PDI knockdown by siRNAs

Results from our earlier studies have led to the suggestion that PDI plays a crucial role in mediating chemically-induced ferroptosis through its ability to catalyze NOS activation (*i.e.*, dimer formation) [23]. In this study, we found that in erastin-treated cells, total iNOS protein level was increased in a dose- and time-dependent manner, although the PDI level was largely unaffected (Fig. 6A, B). Interestingly, it was observed that when the purified PDI protein (at 2 μg/μL) was incubated in vitro with cell lysates prepared from untreated BRL-3A hepatocytes, the stability of the iNOS proteins (including the monomer and dimer iNOS proteins) was increased by the presence of PDI (Fig. 6C, D).

To determine whether PDI plays an important role in mediating erastin-induced ferroptosis in rat hepatocytes, we selectively knocked down PDI expression in these cells using PDI-specific siRNAs. Western blotting results confirmed the effectiveness of PDI knockdown at the protein levels (Fig. 6E). Next, we determined the effect of PDI knockdown on erastin-induced cytotoxicity. We found that PDI knockdown caused a drastic reduction in the sensitivity of rat hepatocytes to erastin-induced cytotoxicity (Fig. 6F). PDI knockdown also attenuated erastin-induced increase in iNOS dimer and monomer levels (Fig. 6G). Similarly, erastin-induced accumulation of cellular NO (Fig. 6H), ROS (Fig. 6I) and lipid ROS (Fig. 6J) was also markedly reduced in cells with PDI knockdown. Moreover, under conditions of PDI knockdown, the protective effect of cystamine (an inhibitor of PDI) against erastin-induced ferroptosis in these hepatocytes was also mostly abrogated (described later). These results provide strong support for the hypothesis that PDI is a crucial upstream mediator of erastin-induced hepatocyte toxicity in vitro.

To provide additional support for the notion that PDI is involved in mediating erastin-induced cell death in BRL-3A rat hepatocytes, we also examined in this study the cytoprotective effect of several known PDI inhibitors, including cystamine, 4-OH-E_1, SNAP and EN460, on erastin-induced ferroptosis as well as their effect on PDI-mediated iNOS dimerization in these cells. The results are briefly summarized below.

Cystamine

Cystamine is a well-known covalent inhibitor of PDI's catalytic activity [37, 38]. We found that cystamine had a strong protective effect against erastin-induced loss of cell viability, with a maximal protection (close to 100%) observed when 50 μM cystamine was present (Fig. 7A, B, Supplementary Fig. S12). In addition, joint treatment of cells with cystamine strongly abrogated erastin-induced accumulation of cellular NO (Fig. 7C, D), ROS (Fig. 7E, F) and lipid-ROS (Fig. 7G, H). While treatment with erastin significantly increased total iNOS protein level, joint treatment with cystamine abrogated erastin-induced increase in iNOS protein level and its dimerization (Fig. 7I, J). In comparison, the cellular PDI protein level was essentially unaffected by treatment with cystamine (Fig. 7I). Notably, when PDI is knocked down, the protective effect of cystamine against erastin-induced cytotoxicity was mostly abrogated (Fig. 7K). This result shows that PDI is the main cellular target that mediates cystamine's cytoprotection against erastin-induced ferroptosis in BRL-3A rat hepatocytes.

4-OH-E_1

4-Hydroxyestrone (4-OH-E_1) is an endogenous metabolite of estrone that can inhibit PDI's catalytic activity [39].

(See figure on next page.)

Fig. 5 Role of lipid-ROS accumulation in erastin-induced ferroptosis in BRL-3A rat hepatocytes. **A** Protective effect of Fer-1 against erastin-induced ferroptotic cell death (MTT assay). Cell viability was assessed after the cells were treated with different concentrations of Fer-1 ± erastin (2.5 μM) for 24 h ($n = 4$), and cell viability was determined by MTT assay. **B**, **C** Protective effect of Fer-1 against erastin-induced accumulation of cellular lipid-ROS (**B** for flow cytometry, $n = 3$; **C** for confocal microscopy, scale bar = 5 μm). Cells were treated with erastin (2.5 μM) ± Fer-1 (100 nM) for 8 h and then stained with BODIPY™-581/591-C11 for flow cytometry (**B**) or confocal microscopy (**C**). **D**, **E**, **F**, **G** Protective effect of Fer-1 against erastin-induced accumulation of cellular NO and ROS (**D**, **F** for fluorescence microscopy, scale bar = 25 μm; **E, G** for flow cytometry, $n = 3$). Quantitative values for **D** and **F** are shown in Supplementary Fig. S6A and S6B. The drug treatment condition was the same as in **B**, **C**. Each value represents the mean ± S.D. ($^{\#}P < 0.05$; ** or $^{\#\#}P < 0.01$; n.s. not significant)

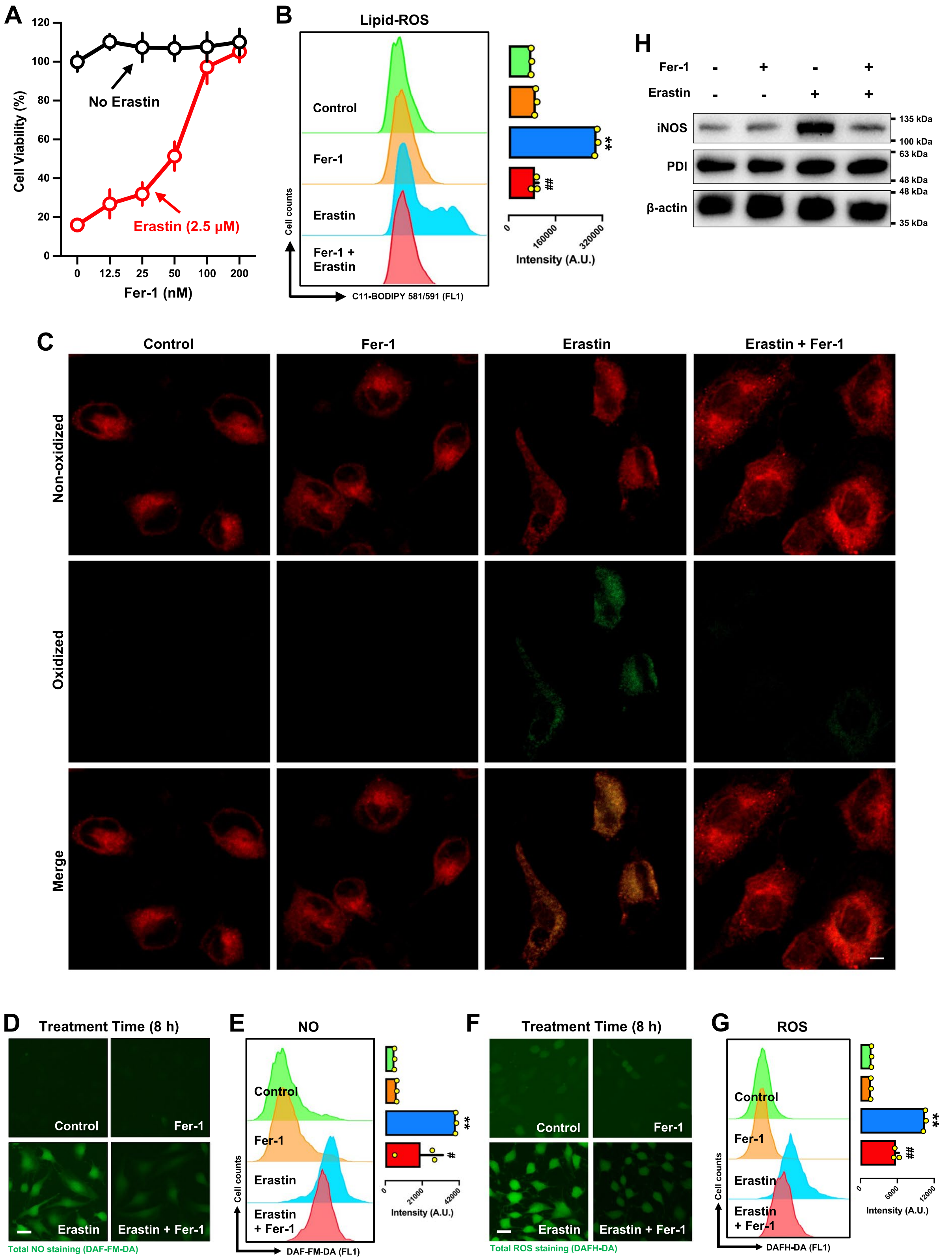

Fig. 5 (See legend on previous page.)

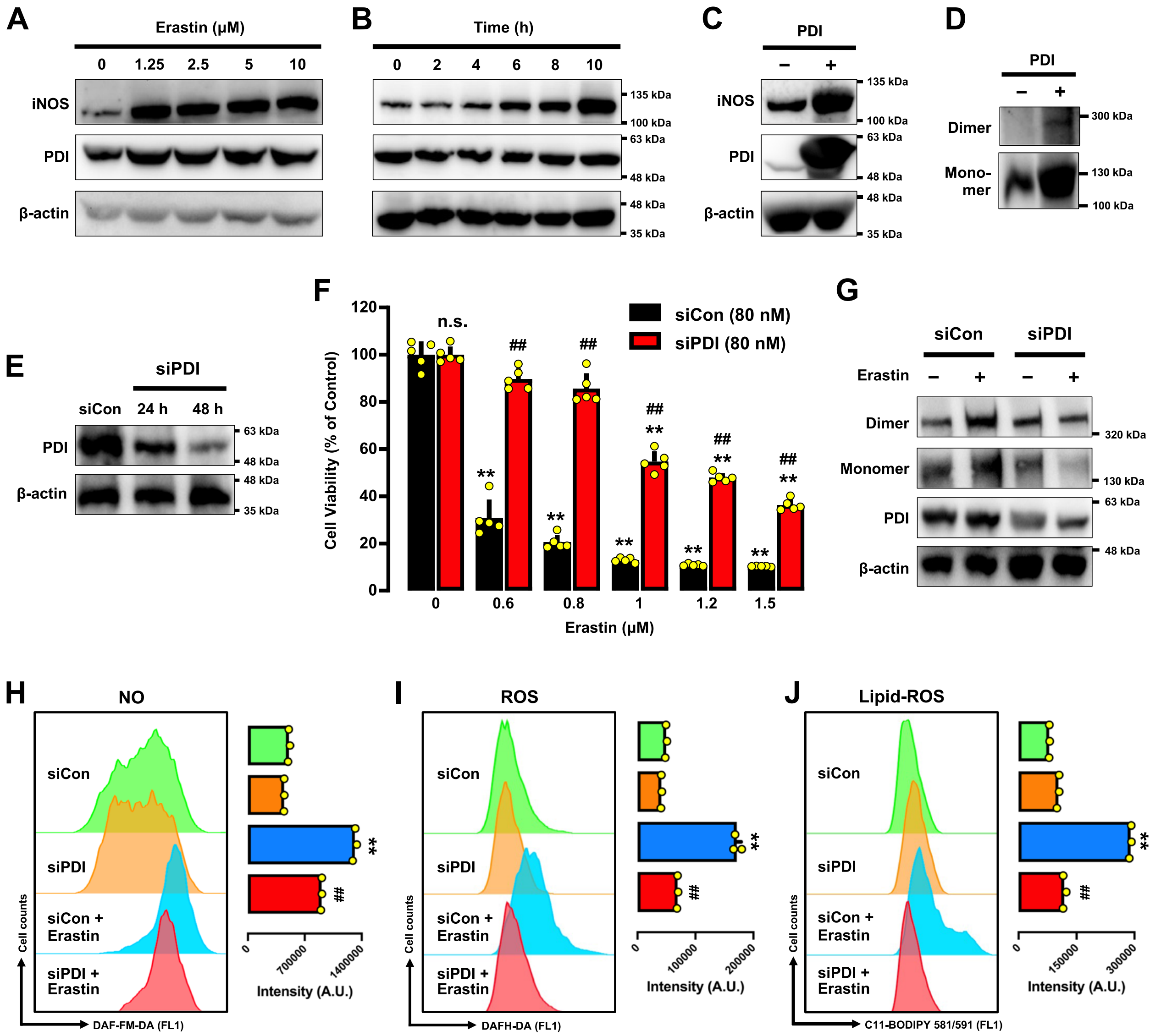

Fig. 6 Effect of PDI knockdown on erastin-induced ferroptosis and accumulation of NO, ROS and lipid-ROS in BRL-3A rat hepatocytes. **A**, **B** Dose- and time-dependent effect of erastin on total iNOS and PDI protein levels (Western blotting). Cells were treated with different concentrations of erastin for 8 h (**A**) or treated with 2.5 μM erastin for different durations as indicated (**B**). The total iNOS and PDI protein levels were determined by SDS-PAGE (with 30 μg protein loaded in each lane).**C**, **D** Effect of purified PDI on the stability of total iNOS and its dimer (Western blotting). Lysates from untreated cells were prepared and then incubated in the presence or absence of purified PDI protein (2 μg/μL) at 4 °C for 1 h. The total iNOS protein (monomer iNOS + dimer iNOS) were separated by SDS-PAGE, while the dimer and monomer forms of iNOS were separated by the non-reducing SDS-PAGE (30 μg proteins were loaded in each lane). **E** PDI protein levels in BRL-3A rat hepatocytes following transfection with the control siRNAs (80 nM) for 48 h or PDI-specific siRNAs for 24 and 48 h (Western blotting). **F** Protective effect of PDI knockdown against erastin-induced ferroptotic cell death (MTT assay). Cells were transfected with the control siRNAs or PDI-specific siRNAs (80 nM) for 48 h, and then cells were treated with increasing concentrations of erastin for an additional 24 h ($n = 5$). **G** Effect of PDI knockdown on erastin-induced change in dimer iNOS, monomer iNOS and PDI protein levels (Western blotting). **H**, **I**, **J** Protective effect of PDI knockdown against erastin-induced accumulation of cellular NO, ROS and lipid ROS (flow cytometry). Cells were transfected with the control siRNAs or PDI-specific siRNAs (80 nM) for 48 h, and then cells were treated with erastin (0.6 μM) for 8 h and subject to flow cytometic analysis of NO (**H**), ROS (**I**) and lipid-ROS (**J**). The left panels are the histograms, and the right panels are the corresponding quantitative intensity values ($n = 3$). Each value represents the mean ± S.D. (** or.$^{\#\#}P < 0.01$; n.s. not significant)

It was recently shown that 4-OH-E_1 has a strong protective effect against GSH depletion-associated ferroptosis in vitro [39]. We found that 4-OH-E_1 had a strong protective effect against erastin-induced ferroptosis in rat hepatocytes (Fig. 8A, Supplementary Fig. S13), and also effectively abrogated erastin-induced accumulation of cellular NO (Fig. 8B, C), ROS (Fig. 8D, E) and lipid-ROS (Fig. 8F, G). In addition, joint treatment of 4-OH-E_1 strongly abrogated erastin-induced increase in total iNOS protein level (Fig. 8H).

SNAP

S-Nitroso-*N*-acetylpenicillamine (SNAP), a thiol-nitrosylating agent [40], was shown earlier to increase *S*-nitrosylation of PDI [24], and the *S*-nitrosylated PDI is catalytically inactive. We found that SNAP partially protected against erastin-induced cell death in rat hepatocytes (MTT assay), while SNAP itself was also toxic to the cells (Fig. 9A, B, Supplementary Fig. S14). In addition, joint treatment of cells with SNAP reduced erastin-induced accumulation of cellular NO (Fig. 9C, D), ROS (Fig. 9E, F) and lipid-ROS (Fig. 9G, H).

EN460

ERO1 is an enzyme that catalyzes the oxidation of PDI [20, 41]. To probe the involvement of ERO1 in ferroptosis, we studied the effect of EN460, a known ERO1α inhibitor [42], on erastin-induced ferroptosis. EN460 exerted a modest protective effect against erastin-induced ferroptosis (based on MTT assay), with a maximal protection of approximately 60% when it was present at 25 μM (Fig. 10A, B, Supplementary Fig. S15). Notably, EN460 was cytotoxic when present alone at 50 μM (Fig. 10A). In addition, EN460 partially abrogated erastin-induced accumulation of cellular NO (Fig. 10C, D), ROS (Fig. 10E, F) and lipid-ROS (Fig. 10G, H). Erastin-induced increase in cellular iNOS protein level was strongly abrogated by joint treatment with EN460 (Fig. 10I), but PDI protein level was unaffected (Fig. 10I).

PDI mediates APAP-induced liver damage in an in vivo mouse model

Gross and histological change

APAP is commonly used to induce liver injury through induction of GSH depletion-associated ferroptosis in hepatocytes in vivo [43–45]. In this study, APAP-induced acute liver injury in male C57BL/6J mice was employed as an in vivo model to investigate the role of PDI in the induction of ferroptotic hepatocyte injury. The mice were treated with APAP (300 mg/kg, gastric intubation) alone or in combination with cystamine (a PDI inhibitor, at 40 mg/kg, *i.p.* injection).

Administration of APAP alone for 24 h caused marked changes in liver surface abnormality and in liver to body weight ratio, and joint treatment of the animals with cystamine exerted a strong protection against these changes (Fig. 11A, B). Histological analysis of H/E-stained liver slides showed that APAP treatment caused extensive hepatocyte death, and severe hepatocyte degeneration was clearly seen around the central vein region of hepatic lobules (Fig. 11C). Typical cellular damage detected under a light microscopy included cellular swollen and ballooning and loss of nuclei (Fig. 11C). Joint treatment of the animals with cystamine exerted a strong protection against APAP-induced hepatocyte injury, and a majority of hepatocytes surrounding the central vein region survived APAP insult (Fig. 11C).

Change in biochemical markers

The plasma GPT and GOT levels were commonly used to reflect the degree of liver injury following APAP treatment. APAP caused marked increase in plasma GPT and GOT levels (approximately 100- and 3-fold higher, respectively) over the control group (Fig. 11D). Joint treatment of the animals with cystamine significantly reduced the GPT and GOT levels (the GOT activity was nearly reduced to the control level).

During APAP-induced hepatocyte toxicity, it is generally believed that the cellular ROS could cause unsaturated fatty acids to produce lipid peroxides, which are slowly broken down into a number of compounds, such as malondialdehyde (MDA). Hence, the change in plasma MDA level was commonly used to reflect the level of lipid peroxidation. We found that the plasma MDA level

(See figure on next page.)

Fig. 7 Role of PDI in mediating iNOS dimer formation and ferroptotic cell death in erastin-treated BRL-3A rat hepatocytes. **A**, **B** Protective effect of cystamine against erastin-induced cell death (**A** for MTT assay; **B** for flow cytometry). In **A**, cell viability was assessed after the cells were treated with different concentrations of cystamine ± erastin (2.5 μM) for 24 h (*n* = 4); in **B**, cells were first treated with erastin (2.5 μM) ± cystamine (50 μM) for 8 h, and then stained with Calcein-AM (200 nM) and PI (50 μg/mL) for an additional 20 min. **C**, **D**, **E**, **F.** Protective effect of cystamine against erastin-induced accumulation of cellular NO and ROS (**C**, **E** for fluorescence microscopy, scale bar = 25 μm; **D**, **F** for flow cytometry, *n* = 3). Cells were treated with erastin (2.5 μM) ± cystamine (50 μM) for 8 h and then stained with DAF-FM-DA (**C**, **D**) and DCFH-DA (**E**, **F**). Quantitative values for **C** and **E** are shown in Supplementary Fig. S16A and S16B. **G**, **H** Protective effect of cystamine against erastin-induced accumulation of cellular lipid-ROS (**G** for confocal microscopy, scale bar = 5 μm; **H** for flow cytometry, *n* = 3). **I**, **J** Effect of cystamine on erastin-induced change in dimer iNOS, monomer iNOS, total iNOS and PDI protein levels (Western blotting). The drug treatment condition was the same as in **B**. **K** Protective effect of cystamine against erastin-induced cell death under conditions of PDI knockdown (MTT assay). Cells were treated with increasing concentrations of cystamine ± erastin (0.6 μM) for 24 h (*n* = 5). Each value represents the mean ± S.D. (** or.$^{\#\#}P < 0.01$; n.s. not significant)

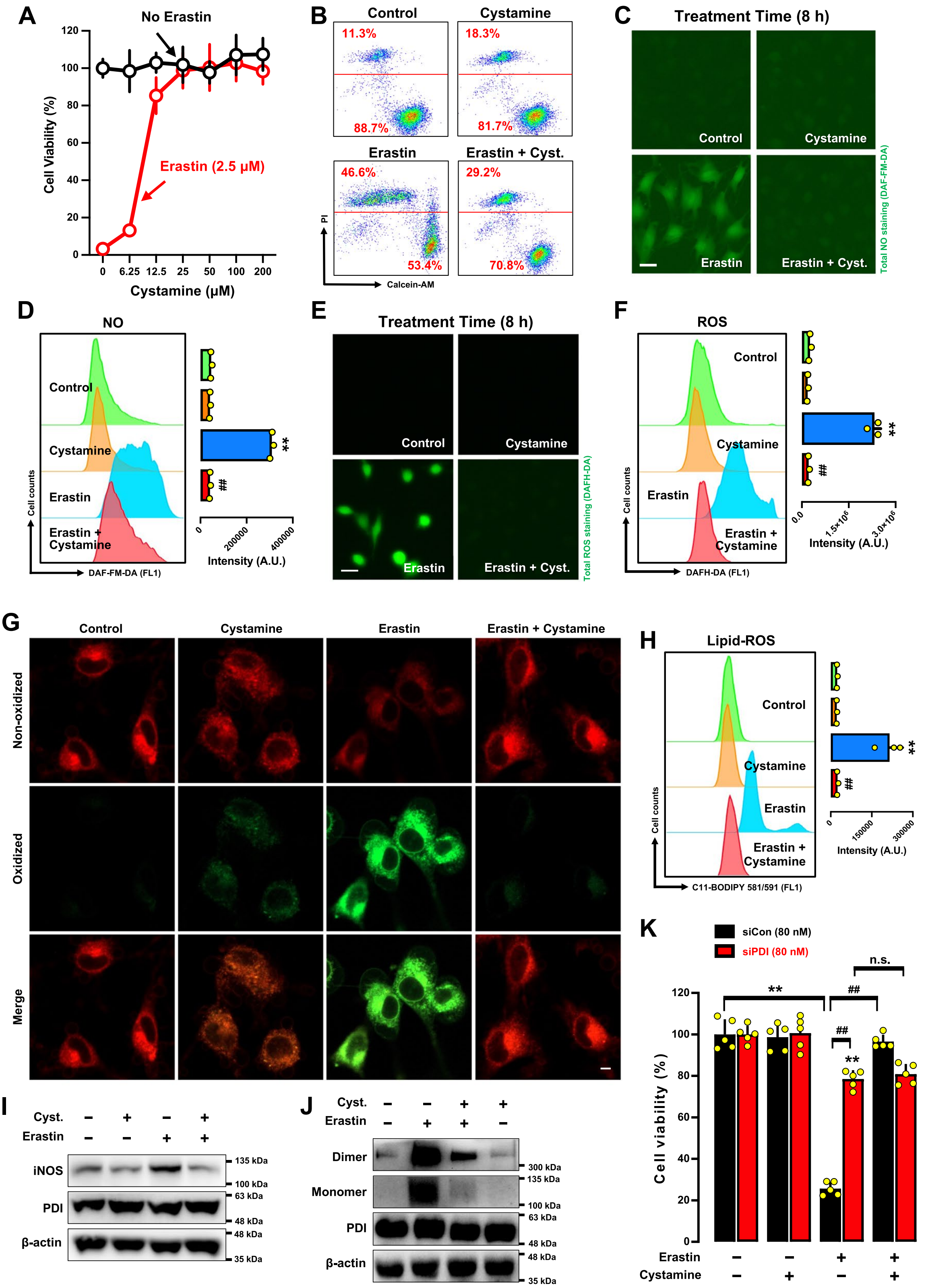

Fig. 7 (See legend on previous page.)

in APAP-treated mice was increased by approximately 3 times, and joint treatment with cystamine abrogated this increase (Fig. 11E).

To probe the role of cellular ROS in APAP-induced hepatocyte toxicity in vivo, fresh mouse liver tissues were harvested for preparation of liver cell suspension. The isolated liver cells were stained for ROS and analyzed by flow cytometry. While 24-h APAP treatment induced ROS accumulation in mouse liver cells in vivo, joint treatment with cystamine abrogated APAP-induced ROS accumulation in these cells (Fig. 11F).

In this study, we also determined the time-dependent change in liver injury following APAP administration for different durations (0, 4, 8 and 24 h). We found that significant abnormalities in the liver surface appearance started to appear at 4 h after APAP treatment, and it became readily visible at 8 h (Fig. 11G). A similar increase in hepatocyte ROS level was also seen at 4 and 24 h (Fig. 11H). In comparison, significant increase in plasma GPT and GOT level was only seen at 24 h, but not at 4 h (Fig. 11I).

Change in CYP2E1 and PDI protein levels

It is known that CYP2E1 is an important hepatic drug-metabolizing enzyme that converts APAP to a hepatotoxic metabolite (NAPQI), and lack of CYP2E1 would make the mice insensitive to APAP-induced hepatotoxicity. Western blot analysis showed that the CYP2E1 protein levels in the liver of control and APAP-treated mice were readily detected, and the protein levels were decreased after APAP exposure for 4 h (Fig. 11J), which likely is associated with APAP-induced hepatocyte injury. In comparison, the PDI protein level was not significantly altered by APAP treatment (Fig. 11J). IHC staining showed that CYP2E1 protein staining was clearly seen in the hepatocytes surrounding the central vein region (Fig. 11K). It is of note that in the control hepatic lobules, there was a clear separation between those cells which surround the central vein and are strongly stained for CYP2E1 protein and those cells which are farther away from the central vein but are not stained for CYP2E1 protein. The distinct sublobular distribution of CYP2E1 is consistent with the localized sublobular hepatocyte injury seen in APAP-treated animals. Notably, the protein level of CYP2E1 in damaged hepatocytes around the central vein of APAP-treated animals was significantly reduced (due to hepatocyte injury); in comparison, in animals jointly treated with cystamine and APAP, the CYP2E1 protein level in hepatocytes around the central vein was not markedly different from that in the control group (Fig. 11K), which is consistent with the lack of severe hepatocyte injury in animals jointly treated with cystamine and APAP.

PDI protein was also readily detected in the hepatocytes, and its level in hepatocytes was markedly reduced in APAP-damaged hepatocytes around the central vein, and joint treatment with cystamine restored its protein levels in these hepatocytes (Fig. 11L). The observations were also consistent with the results from Western blot analysis (Fig. 11M). In this study, the mRNA levels of PDI, ERO1α and GPX4 in different treatment groups were also determined with qRT-PCR, and the results were shown in (Fig. 11N). It was observed that the mRNA levels for PDI and ERO1α were modestly reduced by APAP treatment, and joint treatment with cystamine restored their levels (Fig. 11N). In comparison, the mRNA level for GPX4 was markedly reduced (by approximately 70%) in APAP-treated animals, which is in agreement with an earlier study [12], and joint treatment of the animals with cystamine abrogated the reduction in liver GPX4 mRNA level (Fig. 11N).

Effect of PDI conditional knockdown on APAP-induced hepatocyte injury in vivo

In this study, the hepatocyte-specific homozygous PDI conditional knockout C57BL/6J mice (PDI$^{fl/fl}$ Alb-cre) were prepared in our laboratory and used to examine the effect of PDI deficiency on APAP-induced liver injury as well as on the protective effect of cystamine in vivo. PDI conditional knockout was confirmed by Western blot analysis of liver PDI protein level (Fig. 12A) and by immunohistochemical staining of the liver slides for PDI protein (Fig. 12B). It was evident that the PDI protein level in hepatocytes of PDI$^{fl/fl}$ Alb-cre mice was essentially undetectable compared to the wild-type mice. In addition, qRT-PCR analysis of PDI mRNA in the liver

(See figure on next page.)

Fig. 8 Protective effect of 4-OH-E$_1$ against erastin-induced ferroptosis in BRL-3A rat heptocytes. **A** Protective effect of 4-OH-E$_1$ against erastin-induced loss of cell viability (MTT assay). Cells were treated with increasing concentrations of 4-OH-E$_1$ ± erastin (2.5 μM) for 24 h (*n* = 4). **B**, **C**, **D**, **E** Protective effect of 4-OH-E$_1$ against erastin-induced accumulation of cellular NO and ROS (**B**, **D** for fluorescence microscopy, scale bar = 25 μm; **C**, **E** for flow cytometry, *n* = 3). Cells were treated with erastin (2.5 μM) ± 4-OH-E$_1$ (2.5 μM) for 8 h and then stained with DAF-FM-DA (**B**, **C**) and DCFH-DA (**D**, **E**). Quantitative values for **B** and **D** are shown in Supplementary Fig. S17A and 17B. **F**, **G** Protective effect of 4-OH-E$_1$ against erastin-induced accumulation of cellular lipid-ROS (**F** for flow cytometry, *n* = 3; **G** for confocal microscopy, scale bar = 5 μm). **H** Effect of cystamine on erastin-induced change in total iNOS and PDI protein levels (Western blotting). The drug treatment condition was the same as in **B**, **C**, **D**, **E**. Each value represents the mean ± S.D. (** or.$^{\#\#}P < 0.01$)

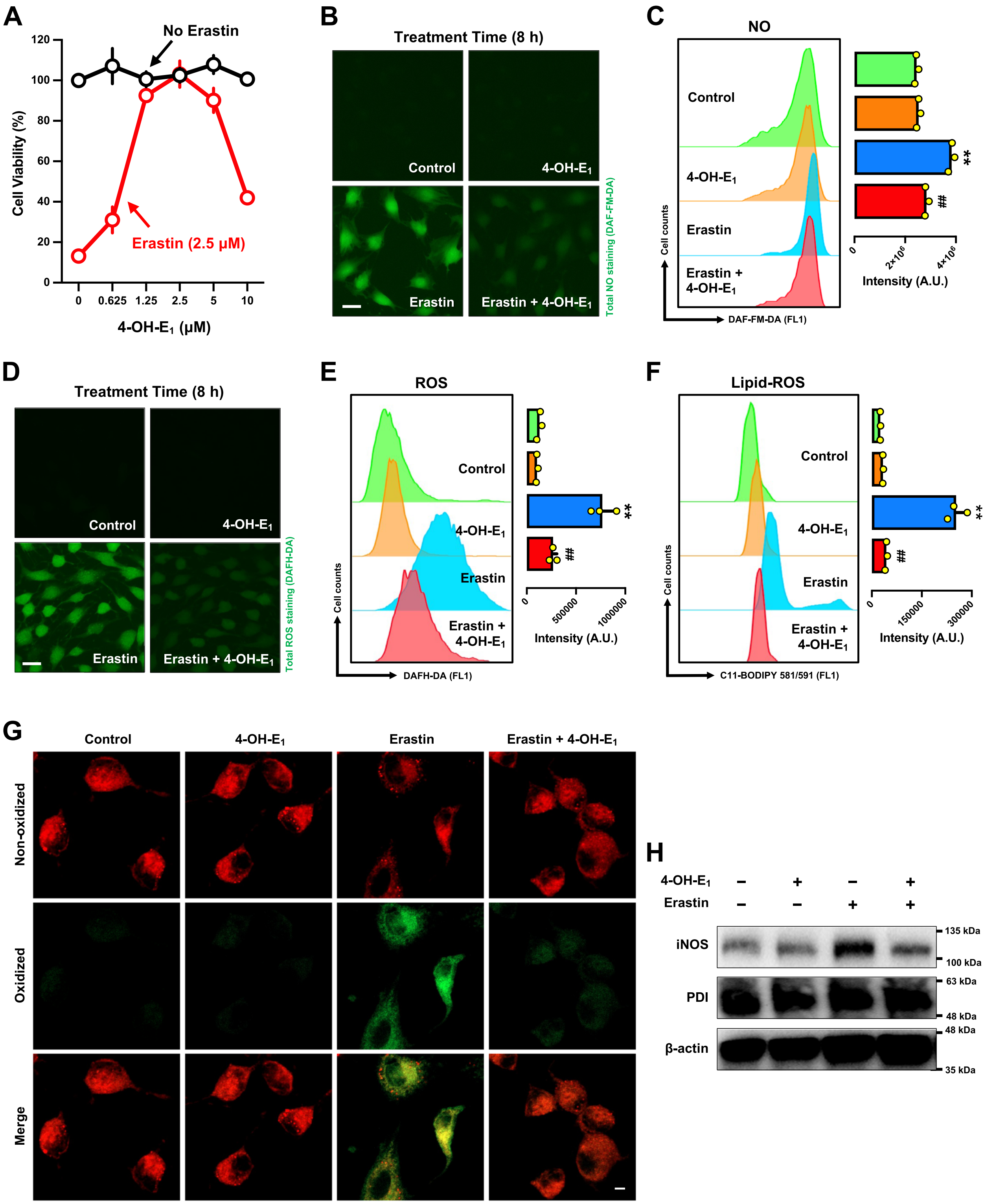

Fig. 8 (See legend on previous page.)

of PDI$^{fl/fl}$ Alb-cre mice also confirmed these findings (Fig. 12C).

Interestingly, the livers of the PDI conditional knockout mice had a pale gross appearance compared to the livers of wild-type mice (Fig. 12D). Histological analysis showed that the hepatocytes of PDI$^{fl/fl}$ Alb-cre mice were full of intracellular vacuole structures (Fig. 12E). The presence of intracellular vacuole structures in PDI$^{fl/fl}$ Alb-cre mice was very different from the hepatocytes of the wild-type animals. After centrifugation of the crude liver homogenates prepared from PDI$^{fl/fl}$ Alb-cre mice, there was a visible layer of "white lipids" floating on top of the centrifugation tubes, whereas such a visible lipid layer was not present in the control liver homogenates (Fig. 12F). Together, these observations suggest the presence of higher lipid contents in the hepatocytes of PDI$^{fl/fl}$ Alb-cre mice compared to those of the wild-type animals.

After the PDI$^{fl/fl}$ Alb-cre mice were treated with APAP alone for 24 h, the gross appearance of their livers was not markedly different from vehicle-treated control animals (Fig. 12D). This was quite different from what was observed in the wild-type animals (refer to Fig. 11A for comparison). While hepatocyte injury was detected in APAP-treated PDI$^{fl/fl}$ Alb-cre mice, the degree of cellular damage was markedly less pronounced compared to the wild-type mice (Fig. 12G). We also compared the change in plasma GPT and GOT levels in the wild-type and PDI$^{fl/fl}$ Alb-cre mice following different treatments. We found that there was no significant difference in APAP-induced increase in plasma GPT levels between the two genotypes, but APAP-induced increase in plasma GOT levels in PDI$^{fl/fl}$ Alb-cre mice was markedly lower than that seen in wild-type mice (Fig. 12H).

We also compared the CYP2E1 protein levels in the livers of both wild-type and PDI$^{fl/fl}$ Alb-cre mice. Western blot analysis showed that the CYP2E1 protein levels in hepatocytes of PDI$^{fl/fl}$ Alb-cre mice were comparable to those found in the wild-type animals (Fig. 12A). Treatment of the animals with APAP slightly reduced the size of CYP2E1-stained region around the central vein, and it was readily visible that there was a small region closest to the central vein which had a reduced CYP2E1 staining (Fig. 12I). The APAP-induced reduction in CYP2E1 staining around the central vein was less severe compared to APAP-induced change in wild-type mice (compared Fig. 12I with Fig. 11K), which is in line with a reduced severity of APAP-induced hepatocyte injury in the PDI$^{fl/fl}$ Alb-cre mice. Here it is of note that while the PDI protein was undetectable in the hepatocytes of the control and APAP-treated PDI$^{fl/fl}$ Alb-cre mice, but it was detected in non-hepatocyte cells (likely endothelial cells or Kupffer cells) (Fig. 12J), and its level in these cells was increased in APAP-treated animals (Fig. 12J). Joint treatment of the animals with cystamine abolished the increase of PDI protein level in these non-hepatocytes (Fig. 12J).

Together, these observations show that the hepatocyte PDI is involved in mediating APAP-induced liver injury in vivo, and pharmacological inhibition of PDI's catalytic activity effectively prevents APAP-induced hepatocyte injury.

Discussion

In our recent studies [22–24], we have shown that during the induction of GSH depletion-associated ferroptotic cell death, there is a time-dependent induction of NO accumulation occurring first, followed by cellular ROS accumulation and finally lipid-ROS accumulation. In the present study, we confirm in cultured hepatocytes that treatment with erastin causes NO accumulation in a concentration- and time-dependent manner, and the increase in cellular NO levels is clearly detectable at approximately 4 h after erastin exposure and peaks at approximately 8 − 10 h. In comparison, the increase of cellular ROS becomes readily detectable at approximately 6 h after erastin treatment, and it is apparent that the increase in cellular ROS level is approximately 2 h behind NO accumulation, which is consistent with our earlier observation [24]. Similarly, we find that the cellular lipid-ROS accumulation is markedly increased by treatment with erastin. Erastin-induced lipid-ROS accumulation becomes detectable after 6 h, reaching a peak at approximately 8 h. Therefore, it is evident that erastin-induced accumulation of cellular NO and ROS/lipid-ROS in hepatocytes also follows a sequential order: cellular NO accumulation occurring first, followed by cellular ROS/lipid-ROS. Provided below is a discussion of the

(See figure on next page.)

Fig. 9 Protective effect of SNAP against erastin-induced ferroptosis in BRL-3A rat hepatocytes. **A**, **B** Protective effect of SNAP against erastin-induced cytotoxicity (**A** for MTT assay; **B** for flow cytometry). In **A**, cells were treated with increasing concentrations of SNAP ± erastin (2.5 μM) for 24 h ($n = 4$); in **B**, cells were treated with erastin (2.5 μM) ± SNAP (50 μM) for 8 h, and then stained with Calcein-AM (200 nM) and PI (50 μg/mL) for an additional 20 min for flow cytometry analysis. **C**, **D**, **E**, **F** Protective effect of SNAP against erastin-induced accumulation of cellular NO and ROS (**C**, **E** for fluorescence microscopy, scale bar = 25 μm; **D**, **F** for flow cytometry, $n = 3$). Quantitative values for **C** and **E** are shown in Supplementary Fig. S18A and S18B. **G**, **H** Protective effect of SNAP against erastin-induced accumulation of cellular lipid-ROS (**G** for confocal microscopy, scale bar = 5 μm; **H** for flow cytometry, $n = 3$). The drug treatment condition was the same as in **B**. Each value represents the mean ± S.D. (** or.$^{\#\#}P < 0.01$)

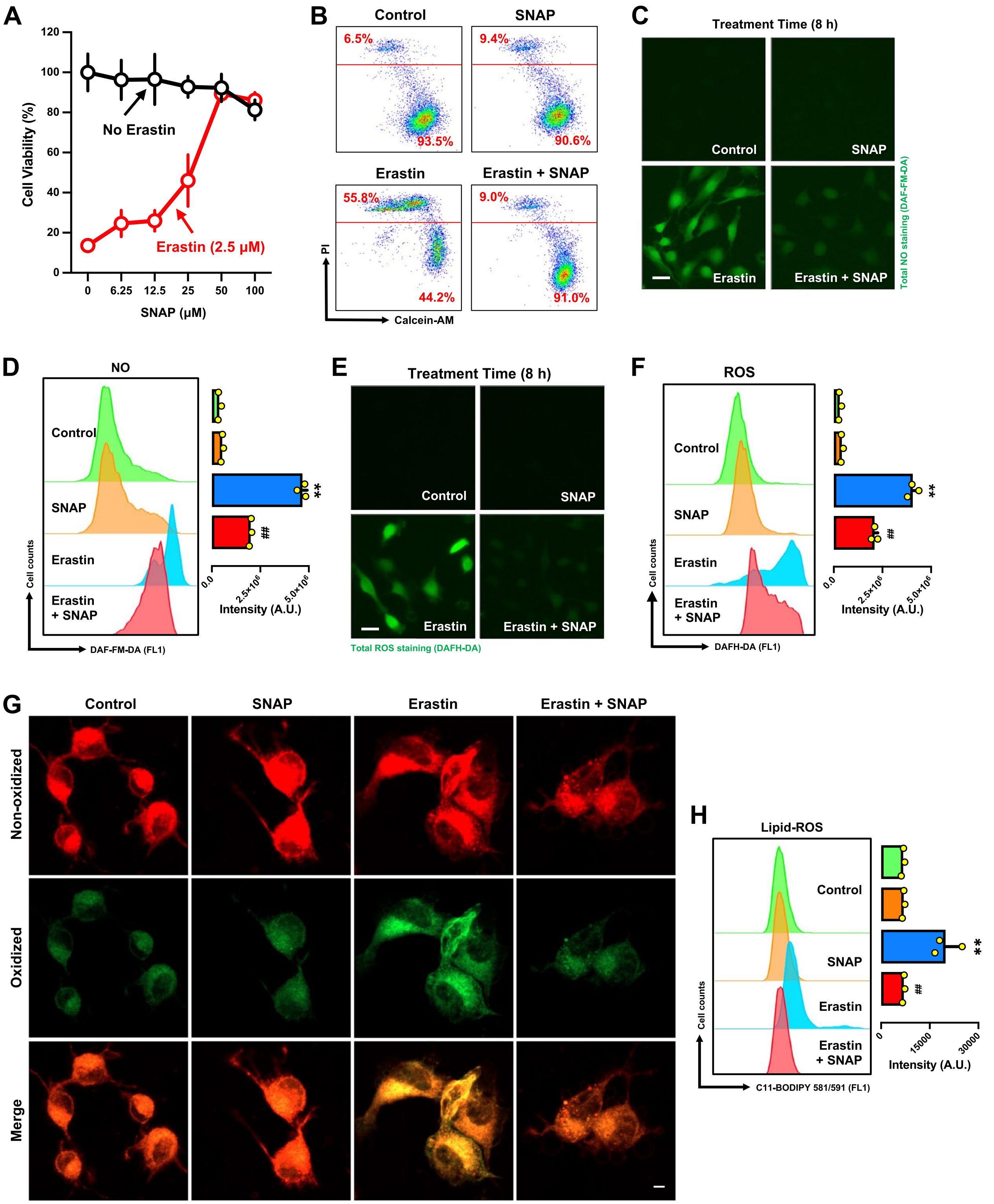

Fig. 9 (See legend on previous page.)

experimental evidence obtained in this study that offers support for the proposed role of cellular NO, ROS/lipid-ROS and PDI in mediating erastin-induced ferroptosis in cultured hepatocytes.

First, there are several lines of evidence in support of the involvement of cellular NO in erastin-induced ferroptosis. ***i***. Erastin treatment causes a concentration- and time-dependent increase in iNOS protein levels (Western blotting). The time-dependent increase in iNOS protein level peaks at around 10 h after erastin exposure. ***ii***. SMT, an inhibitor of iNOS [32], exerts a protective effect against erastin-induced ferroptosis in hepatocytes, and also abrogates erastin-induced accumulation of cellular NO, ROS and lipid-ROS. In addition, SMT also abrogates erastin-induced increase in iNOS protein level, but does not affect total PDI protein level. ***iii***. Joint treatment of cells with SNP, which can release NO inside a cell [30], enhances erastin-induced cytotoxicity, and this cytotoxicity-enhancing effect of SNP is associated with enhanced accumulation of cellular ROS and lipid-ROS, which occurs approximately 2 h earlier compared to their accumulation when erastin is used alone. ***iv***. cPTIO, a known NO scavenger [31], provides a strong protection against erastin-induced cytotoxicity, along with a reduction in cellular NO, ROS and lipid-ROS levels. In addition, cPTIO abrogates erastin-induced increase in iNOS protein level, whereas PDI protein level is unaffected. Together, these observations strongly support the proposed role of iNOS and NO in mediating erastin-induced ferroptotic cell death in cultured hepatocytes.

Second, there is also experimental evidence in support of the involvement of cellular ROS and lipid-ROS in erastin-induced ferroptosis. ***i***. *N*-Acetyl-*L*-cysteine (NAC) is a powerful antioxidant and ROS scavenger [34, 35]. Joint treatment of cells with NAC strongly protects against erastin-induced cell death, which is associated with an abrogation of erastin-induced accumulation of cellular NO, ROS and lipid-ROS. In addition, NAC abrogates erastin-induced increase in cellular iNOS protein, which might explain its abrogation of erastin-induced increase in cellular NO level. ***ii***. Fer-1, a lipid-ROS scavenger and also a potent ferroptosis inhibitor [36], strongly protects against erastin-induced ferroptosis, and this protective effect is associated with a strong reduction in lipid-ROS accumulation and a partial reduction in cytosolic ROS accumulation. Interestingly, it is observed that Fer-1 also partially abrogates erastin-induced NO accumulation. This effect might be due to the fact that Fer-1 also significantly reduces erastin-induced upregulation of total iNOS protein, which may contribute to the observed reduction in cellular NO accumulation. ***iii.*** Similarly, Trolox, a highly-lipophilic compound with preferential scavenging activity for lipid-ROS [33], exerts a quite strong protection against erastin-induced cell death, and this effect is associated with a strong abrogation of erastin-induced accumulation of lipid-ROS and ROS accumulation. Interestingly, Trolox also elicits a rather strong reduction of erastin-induced NO accumulation. This effect of Trolox on NO levels may partly result from its strong reduction of cellular ROS levels (including both cytosolic ROS and lipid-ROS), which would favor the maintenance of cellular GSH levels and thus reduce PDI activation and iNOS dimerization, along with reduced NO accumulation. Jointly, these observations offer support for the notion that accumulation of cellular NO subsequently leads to accumulation of cellular ROS and lipid-ROS in mediating erastin-induced ferroptotic cell death in cultured hepatocytes.

Here it is of note that while the use of lipid-ROS and ROS scavengers would still be highly effective in protecting against chemically-induced ferroptosis both in vitro and in vivo, it does not necessarily mean that these scavengers are better choices for the prevention of chemically-induced ferroptosis. Given that the amount of downstream participating elements (such as cellular lipid-ROS and ROS) are usually formed in much larger quantities, it would be relatively more difficult to effectively remove their impact through the use of another scavenging chemical. On the other hand, the upstream mediators (such as PDI and iNOS) are usually present in much smaller quantities, and it would be far easier and more effective pharmacologically to suppress or remove their impact through the use of chemical inhibitors.

Third, there is considerable experimental evidence obtained in this study which offers support for an

(See figure on next page.)

Fig. 10 Protective effect of EN460 against erastin-induced ferroptosis in BRL-3A rat hepatocytes. **A**, **B** Protection by EN460 against erastin-induced cytotoxicity (**A** for MTT assay; **B** for flow cytometry). In **A**, cells were treated with different concentrations of EN460 ± erastin (2.5 μM) for 24 h ($n = 4$); in **B**, cells were first treated with erastin (2.5 μM) ± EN460 (25 μM) for 8 h and then stained with Calcein-AM (200 nM) and PI (50 μg/mL) for an additional 20 min. **C**, **D**, **E**, **F** Protective effect of EN460 against erastin-induced accumulation of NO and ROS (**C**, **E** for fluorescence microscopy, scale bar = 25 μm; **D**, **F** for flow cytometry, $n = 3$). Quantitative values for **C** and **E** are shown in Supplementary Fig. S19A and S19B. **G**, **H** Protective effect of EN460 against erastin-induced accumulation of lipid-ROS (**G** for confocal microscopy, scale bar = 5 μm; **H** for flow cytometry, $n = 3$). **I** Effect of EN460 on erastin-induced change in total iNOS and PDI protein levels (Western blotting). The drug treatment condition was the same as in **B**. Each value represents the mean ± S.D. (** or.$^{\#\#}P < 0.01$)

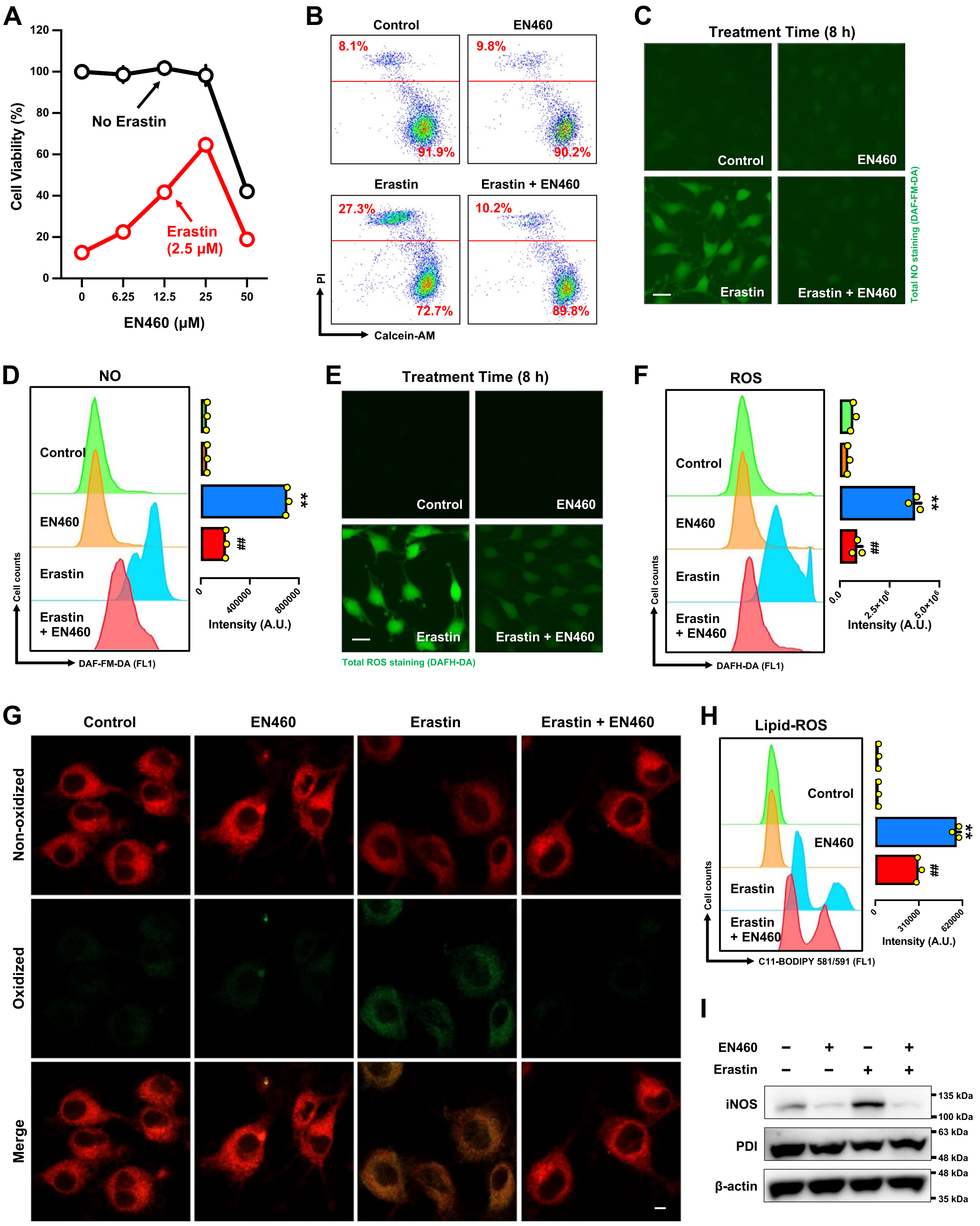

Fig. 10 (See legend on previous page.)

important role of PDI in mediating erastin-induced ferroptosis in rat hepatocytes:

i. Our earlier studies have led to the suggestion that PDI plays a role in mediating chemically-induced ferroptosis through its catalysis of NOS dimer formation [23]. In the present study, it is shown that the stability of total iNOS proteins (*i.e.*, monomer + dimer iNOS) in the in vitro incubation mixture is increased by the presence of PDI, and similarly, the monomer and dimer iNOS protein levels are also increased by PDI. The ability of PDI to stabilize cellular NOS proteins (including its dimer) may offer a partial explanation for the observation that during chemically-induced ferroptosis, there is almost always an increase in cellular NOS protein levels (including both total NOS protein and its dimer levels).

ii. To provide additional support for the involvement of PDI in erastin-induced ferroptosis, we find that cystamine, a known PDI inhibitor [37, 38], exerts a strong protection against erastin-induced ferroptosis in hepatocytes, along with a strong abrogation of NO, ROS and lipid-ROS accumulation. However, under experimental conditions of PDI knockdown in rat hepatocytes, the cytoprotective effect of cystamine was mostly abrogated, clearly suggesting that PDI is a target protein that mediates its cytoprotective effect against chemically-induced ferroptosis.

Here it should be noted that the strong abrogation of cellular NO and ROS/lipid-ROS accumulation by cystamine is clearly not due to its direct free radical-scavenging activity because this small chemical ($NH_2CH_2CH_2–S–S–CH_2CH_2NH_2$) is not a reducing agent at all; in fact, it is a weak oxidizing agent (like GSSG). Its inhibition of PDI is purely due to its ability to covalently modify the free –SH group(s) in PDI's catalytic site, resulting in the formation of $PDI–S–S–CH_2CH_2NH_2$. The drastic protection by cystamine highlights not only the crucial role of PDI in erastin-induced ferroptotic cell death, but also its importance as a mechanistic target for ferroptosis protection.

iii. 4-OH-E_1 is an endogenous inhibitor of PDI's catalytic activity [39]. Recently, it was shown that 4-OH-E_1 can strongly protect against GSH depletion-associated ferroptosis in vitro [39]. In this study, we find that 4-OH-E_1 exerts a strong protection against erastin-induced cell death in rat hepatocytes. The protective effect of 4-OH-E_1 is associated with its strong protection against erastin-induced accumulation of cellular NO, ROS and lipid-ROS.

iv. *S*-Nitroso-*N*-acetylpenicillamine (SNAP), a protein thiol-nitrosylating agent [40] previously reported to increase PDI *S*-nitrosylation [40], is also used in this study to explore the role of PDI *S*-denitrosylation in modulating erastin-induced ferroptosis in rat hepatocytes. We find that while SNAP itself is cytotoxic at high concentrations, joint treatment of cells with SNAP exerts a quite strong protection against erastin-induced cell death, along with partial abrogation of erastin-induced accumulation of cellular NO, ROS and lipid-ROS. SNAP also strongly abrogates erastin-induced increase in cellular iNOS levels.

v. ERO1 is an enzyme that catalyzes the activation (*i.e.*, oxidation) of PDI [20, 41]. We find that EN460, an inhibitor of ERO1, exerts a modest protective effect against erastin-induced ferroptosis, along with a partial abrogation of erastin-induced accumulation of cellular NO, ROS and lipid-ROS. In addition, EN460 abrogates erastin-induced increase in cellular iNOS protein levels.

Collectively, the above observations provide strong support for the hypothesis that PDI plays an important role in mediating erastin-induced ferroptosis in rat hepatocytes through its ability to catalyze iNOS activation (*i.e.*, dimerization) and its ability to increase the

(See figure on next page.)

Fig. 11 Role of PDI in APAP-induced liver damage in wild-type C57BL/6J mice. **A**, **B**, **C**, **D**, **E**, **F.** Protective effect of cystamine against APAP-induced hepatocyte injury in C57BL/6J mice. After fasting for 12 h, the male C57BL/6J mice were treated with APAP (300 mg/kg, gastric intubation) ± cystamine (40 mg/kg, *i.p.*) for an additional 24 h. **A** for liver gross morphology; **B** for liver/body weight ratio ($n = 10$); **C** for H/E staining, upper panel scale bar = 500 μm, lower panel scale bar = 50 μm; **D** for plasma GPT and GOT levels ($n = 3$); **E** for hepatic MDA levels ($n = 3$). Fresh liver samples (approximately 20 mg) were taken and weighed, stained with DCFH-DA (20 μM) for 50 min, and then analyzed by flow cytometry (**F**, $n = 3$). **G** Time-dependent change in liver gross appearance in animals treated with APAP (300 mg/kg) alone. **H**, **I** Change in liver ROS levels and GPT and GOT levels in C57BL/6J mice treated with APAP for different durations (**H** for flow cytometry, $n = 5$; **I** for GPT and GOT levels, $n = 5$. **J** PDI protein levels in animals treated with APAP (300 mg/kg) alone for 4 and 8 h (Western blotting). **K**, **L** IHC staining of CYP2E1 and PDI protein in hepatocytes of C57BL/6J mice treated with APAP for 24 h (**K** for IHC staining of CYP2E1 protein; **L** for IHC staining of PDI protein). The lower panels are the enlarged images of the selected regions in the upper panels (the scale bar for upper panels = 500 μm, and the scale bar for lower panels = 50 μm). **M** PDI protein levels (Western blotting) in the livers of C57BL/6J mice treated with APAP (300 mg/kg) + cystamine (40 mg/kg, *i.p.*) for 24 h. **N** Change in mRNA levels of PDI, ERO1 and GPX4 (determined by qRT-PCR, $n = 5$). Animal treatments were the same as in **A**. Each value represents the mean ± S.D. (* or $^{\#}P < 0.05$; ** or.$^{\#\#}P < 0.01$; n.s. not significant)

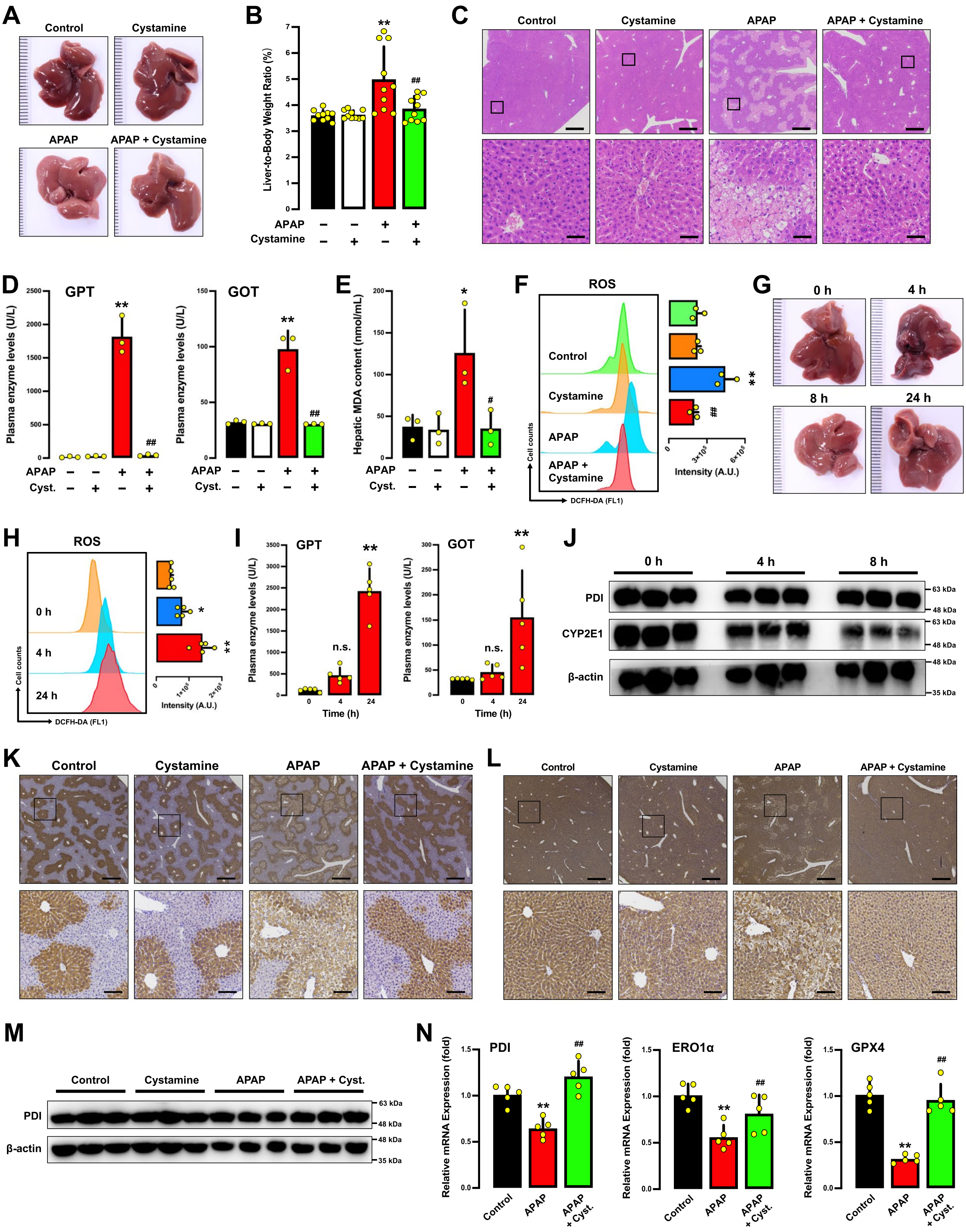

Fig. 11 (See legend on previous page.)

stability of iNOS proteins, which then jointly leads to accumulation of cellular NO and ROS/lipid-ROS, and ultimately ferroptotic cell death.

Lastly, several lines of experimental evidence from animal studies are also provided in this study which jointly offers strong support for the involvement of PDI in mediating APAP-induced liver injury in vivo:

i. APAP is a commonly-used inducer of liver injury through the induction of GSH depletion-associated oxidative cell death in hepatocytes [43–45]. In this study, we show that administration of APAP alone for 24 h induces significant liver injury in mice, which is reflected by change in plasma GPT and GOT activities and plasma MDA level (a biomarker used to reflect the level of lipid peroxidation). We find that joint treatment of animals with cystamine, a PDI inhibitor, elicits a strong protection against APAP-induced hepatocyte injury. The observations made in vivo are in agreement with the observations made in cell culture experiments.

ii. We have shown that treatment with APAP induces ROS accumulation in mouse hepatocytes in vivo, and joint treatment with cystamine abrogates APAP-induced ROS accumulation in these cells.

iii. We have developed the hepatocyte-specific homozygous PDI conditional knockout C57BL/6J mouse model (PDI$^{fl/fl}$ Alb-cre) to examine the effect of PDI deficiency on APAP-induced liver injury as well as on the protective effect of cystamine in vivo. We find that selective PDI deficiency in hepatocytes confers a strong protection against APAP-induced hepatocyte injury compared to the wild-type mice. Joint treatment of the PDI$^{fl/fl}$ Alb-cre mice with APAP and cystamine exerts a relatively mild protection against APAP-induced liver injury. The reason for the less pronounced protective effect of cystamine in APAP-treated, PDI-deficient mice is mostly because APAP only induces very mild liver injury in these animals.

iv. It is of note that in this study, we have also compared the change in plasma GPT and GOT activities in the wild-type and PDI$^{fl/fl}$ Alb-cre mice following APAP treatment. While APAP-induced increase in plasma GPT level is not significantly different in these two genotypes, the GOT level in APAP-treated PDI$^{fl/fl}$ Alb-cre mice is significantly lower than the level seen in APAP-treated wild-type mice. The underlying reason for this discrepancy likely is related to the fact that GPT is mostly a cytosolic enzyme, whereas GOT is mostly associated with the mitochondria (although the cytosol also contains a small amount of this enzyme) [46]. Because of this difference, it is speculated that following APAP-induced liver injury, a marked increase in plasma GPT level likely is more readily seen, whereas an increase in plasma GOT level is only on display when the liver injury is much severer which involves damage to the mitochondria. Therefore, in APAP-treated wild-type animals, both plasma GPT and GOT levels are increased, which reflects a high severity of liver injury seen in these animals; in comparison, in APAP-treated PDI$^{fl/fl}$ Alb-cre mice, the plasma GPT level is increased but the GOT level is only very mildly increased (to a much smaller degree compared to the wild-type mice), which reflects a markedly lower severity of liver injury seen in these transgenic animals.

Together, these observations show that PDI is crucially involved in mediating APAP-induced liver injury in vivo, and pharmacological inhibition of PDI's activity can effectively prevent this injury. Interestingly, the observations made in this study also suggest that the change in plasma GPT level likely is a more sensitive biomarker for chemically-induced liver damage, whereas the increase in plasma GOT level may better reflect the degree of mitochondrial damage in injured hepatocytes in vivo.

Lastly, it is worth noting that there are seven known PDI proteins in the PDI gene family, which include PDIA1 (commonly referred to as PDI) [14], PDIA2 (also called

(See figure on next page.)

Fig. 12 Protective effect of PDI conditional knockout against APAP-induced liver damage in PDI$^{fl/fl}$ Alb-cre mice. **A** Change in hepatocyte CYP2E1 and PDI protein levels in wild-type and PDI$^{fl/fl}$ Alb-cre C57BL/6J mice following APAP treatment (Western blotting). **B**, **C** Differences in PDI in protein levels (**B**) and mRNA levels (**C**) of in wild-type and PDI$^{fl/fl}$ Alb-cre mice (**B** for IHC staining, scale bar = 100 μm; **C** for q-PCR, *n* = 5). **D** Protective effect of cystamine against APAP-induced hepatocyte damage in PDI$^{fl/fl}$ Alb-cre C57BL/6J mice (gross morphology). **E** Comparison of the histological changes (H/E staining) of APAP-induced hepatocyte injury in wild-type and PDI$^{fl/fl}$ Alb-cre C57BL/6J mice. Scale bar in the upper panels = 500 μm, and the scale bar in the lower panels = 50 μm. **F** Difference in the supernatant fractions following centrifugation of liver homogenates prepared from wild-type and PDI$^{fl/fl}$ Alb-cre C57BL/6J mice. **G** Histological change in the liver of wild-type and PDI$^{fl/fl}$ Alb-cre C57BL/6J mice following APAP alone treatment (H/E staining). Scale bar in the upper panels = 500 μm, and the scale bar in the lower panels = 50 μm. **H** Comparison of the changes in plasma GPT and GOT levels in wild-type and PDI$^{fl/fl}$ Alb-cre C57BL/6J mice treated with APAP. **I**, **J** Effect of cystamine on APAP-induced liver injury in PDI$^{fl/fl}$ Alb-cre C57BL/6J mice (Left panels for IHC staining of CYP2E1 protein, scale bar = 500 μm; right panels for IHC staining of PDI protein, scale bar = 100 μm). The treatment was same as in Fig. 11K, L. Each value represents the mean ± S.D. (** or $^{\#\#}P < 0.01$; n.s. not significant)

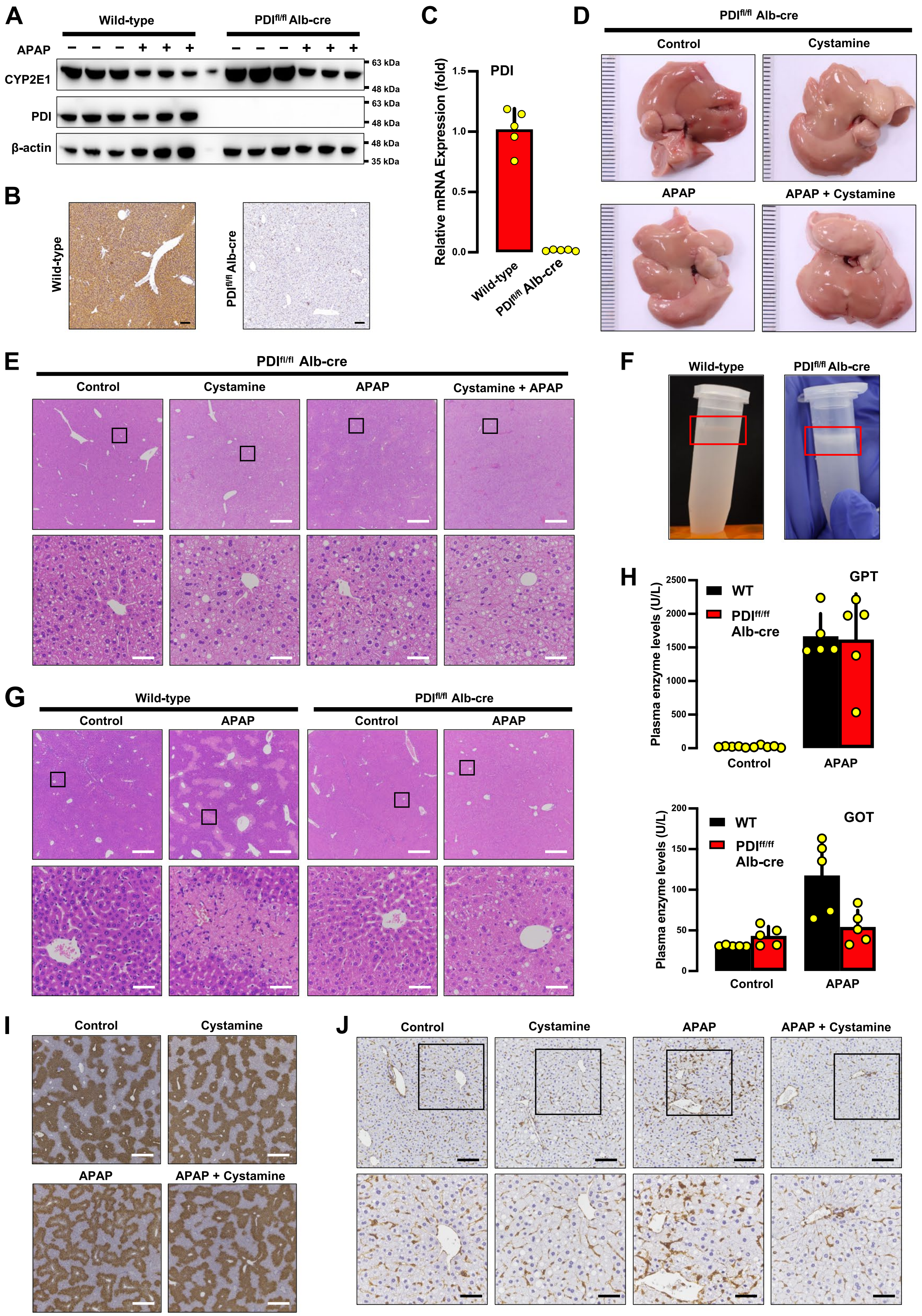

Fig. 12 (See legend on previous page.)

PDIp, a pancreas-specific PDI) [47], PDIA3 [48], PDIA4 [49], PDIA5 [50], PDIA6 [50] and PDILT [51]. Earlier studies have reported that PDI, PDIA3, PDIA4 and PDIA6 are expressed in many cell types [52–58]. Interestingly, a recent study reported that a conserved extracellular domain of the MET oncogene product also contains two CXXC motifs found in PDI, and this extracellular domain displays disulfide isomerase activity [59]. While it is demonstrated in this study that PDI (PDIA1) plays an important role in mediating erastin-induced ferroptotic cell death in rat hepatocytes, it is not known whether other PDI family proteins partially share a similar function in mediating chemically-induced ferroptotic cytotoxicity. Certainly, it will be of future interest to explore these potential possibilities.

Conclusions

As summarized in Supplementary Fig. S20, we confirm in cultured BRL-3A rat hepatocytes that treatment with erastin causes accumulation of cellular NO and ROS/lipid-ROS in a concentration- and time-dependent manner, and their accumulation followed a sequential order, *i.e.*, cellular NO accumulation occurs first, which is followed by ROS/lipid-ROS accumulation. Detailed experimental evidence is provided to show that cellular NO, ROS and lipid-ROS each play a critical role in mediating erastin-induced ferroptosis. In addition, evidence is provided to show that PDI is an upstream mediator of erastin-induced ferroptosis through its ability to catalyze iNOS activation (dimerization) and its ability to increase the stability of iNOS proteins (monomers and dimers). These two effects then jointly lead to accumulation of cellular NO, ROS and lipid-ROS, and ultimately ferroptotic cell death. Using both the wild-type C57BL/6J mice and the PDI conditional knockout (PDI$^{fl/fl}$ Alb-cre) mice, experimental evidence is also provided in this study to show that PDI is crucially involved in mediating APAP-induced liver injury in vivo. Pharmacological inhibition of PDI function can effectively abrogate chemically-induced ferroptotic cell death in vitro and in vivo. Collectively, the results of this study demonstrate that PDI is an important upstream mediator of chemically-induced, GSH depletion-associated hepatocyte ferroptosis, and inhibition of PDI can effectively prevent such injury both in vitro and in vivo.

Supplementary Information

The online version contains supplementary material available at https://doi.org/10.1186/s12964-024-01798-1.

Supplementary Material 1: Supplementary Fig. S1. Dose-dependent induction of cell death by erastin in BRL-3A rat hepatocytes. Cells were seeded in 96-well plates at 2000 cells/well, and 12 h later, they were treated with different concentrations of erastin for an additional 24 h. Cell viability was determined by MTT assay (n = 5). The data shown in A, B and C were obtained from different experiments at different times. Considerable variations in the sensitivity of the cultured rat hepatocytes to erastin's cytotoxicity were noted. Each value represents the mean ± S.D. (** P < 0.01; n.s. not significant). Supplementary Fig. S2. Corresponding quantitative values for the data shown in Fig. 1B–L. Each value is the mean ± S.D. (n =3). (* P < 0.05; **P < 0.01; n.s. not significant). Supplementary Fig. S3. Corresponding quantitative values for the data shown in Fig. 2E, F, I, K. Each value is the mean ± S.D. (n =3). (** or $^{\#\#}P$< 0.01; n.s. not significant). Supplementary Fig. S4. Corresponding quantitative values for the data shown in Fig. 3C, E. Each value is the mean ± S.D. (n =3). (** or $^{\#\#}P$< 0.01). Supplementary Fig. S5. Corresponding quantitative values for the data shown in Fig. 4C, E, K, M. Each value is the mean ± S.D. (n =3). (** or $^{\#\#}P$ < 0.01). Supplementary Fig. S6. Corresponding quantitative values for the data shown in Fig. 5D, F. Each value is the mean ± S.D. (n =3). (** or $^{\#\#}P$ < 0.01). Supplementary Fig. S7. Protective effect of cPTIO against erastin-induced ferroptotic cell death (gross morphological change). Cells were jointly treated with erastin (2.5 μM) ± cPTIO (100 μM) for 24 h, and cellular images were captured with a Nikon Eclipse Ti-U inverted microscope (20×, scale bar = 30 μm). Supplementary Fig. S8. Protective effect of SMT against erastin-induced ferroptotic cell death (gross morphological change). Cells were jointly treated with erastin (2.5 μM) ± SMT (400 μM) for 24 h, and cellular images were captured with a Nikon Eclipse Ti-U inverted microscope (20×, scale bar = 30 μm). Supplementary Fig. S9. Protective effect of Trolox against erastin-induced ferroptotic cell death (gross morphological change). Cells were jointly treated with erastin (2.5 μM) ± Trolox (100 μM) for 24 h, and cellular images were captured with a Nikon Eclipse Ti-U inverted microscope (20×, scale bar = 30 μm). Supplementary Fig. S10. Protective effect of NAC against erastin-induced ferroptotic cell death (gross morphological change). Cells were jointly treated with erastin (2.5 μM) ± NAC (400 μM) for 24 h, and cellular images were captured with a Nikon Eclipse Ti-U inverted microscope (20×, scale bar = 30 μm). Supplementary Fig. S11. Protective effect of Fer-1 against erastin-induced ferroptotic cell death (gross morphological change). Cells were jointly treated with erastin (2.5 μM) ± Fer-1 (100 nM) for 24 h, and cellular images were captured with a Nikon Eclipse Ti-U inverted microscope (20×, scale bar = 30 μm). Supplementary Fig. S12. Protective effect of Cystamine against erastin-induced ferroptotic cell death (gross morphological change). Cells were jointly treated with erastin (2.5 μM) ± cystamine (50 μM) for 24 h, and cellular images were captured with a Nikon Eclipse Ti-U inverted microscope (20×, scale bar = 30 μm). Supplementary Fig. S13. Protective effect of 4-OH-E_1 against erastin-induced ferroptotic cell death (gross morphological change). Cells were jointly treated with erastin (2.5 μM) ± 4-OH-E_1 (2.5 μM) for 24 h, and cellular images were captured with a Nikon Eclipse Ti-U inverted microscope (20×, scale bar = 30 μm). Supplementary Fig. S14. Protective effect of SNAP against erastin-induced ferroptotic cell death (gross morphological change). Cells were jointly treated with erastin (2.5 μM) ± SNAP (50 μM) for 24 h, and cellular images were captured with a Nikon Eclipse Ti-U inverted microscope (20×, scale bar = 30 μm). Supplementary Fig. S15. Protective effect of EN460 against erastin-induced ferroptotic cell death (gross morphological change). Cells were jointly treated with erastin (2.5 μM) ± EN460 (25 μM) for 24 h, and cellular images were captured with a Nikon Eclipse Ti-U inverted microscope (20×, scale bar = 30 μm). Supplementary Fig. S16. Corresponding quantitative values for the data shown in Fig. 7C, E. Each value is the mean ± S.D. (n =3). (** or $^{\#\#}P$ < 0.01). Supplementary Fig. S17. Corresponding quantitative values for the data shown in Fig. 8B, D. Each value is the mean ± S.D. (n =3). (** or $^{\#\#}P$ < 0.01). Supplementary Fig. S18. Corresponding quantitative values for the data shown in Fig. 9C, E. Each value is the mean ± S.D. (n =3). (** or $^{\#\#}P$ < 0.01). Supplementary Fig. S19. Corresponding quantitative values for the data shown in Fig. 10C, E. Each value is the mean ± S.D. (n =3). (** or $^{\#\#}P$ < 0.01). Supplementary Fig. S20. Schematic illustration of the mechanism by which PDI plays an important contributing role in mediating erastin- and APAP-induced ferroptotic hepatocyte death *in vitro* and *in vivo*. Please refer to the Discussion section for detailed explanation.

Authors' contributions

Bao-Ting Zhu: Conceptualization, Methodology, Formal analysis, Resources, Writing—Original Draft, Writing—Review & Editing, Supervision, Project administration, Funding acquisition. Yan-Yin Zhu: Methodology, Validation, Formal analysis, Investigation, Data Curation, Writing—Original Draft. Qi Zhang: Methodology, Validation, Investigation. Yi-Chen Jia: Methodology, Validation. Ming-Jie Hou: Methodology, Validation.

Funding

This study was supported, in part, by research grants from Shenzhen Peacock Plan (No. KQTD2016053117035204), Shenzhen Key Laboratory of Steroidal Drug Research (No. ZDSYS20190902093417963), Shenzhen Bay Laboratory (No. SZBL2019062801007) and the National Natural Science Foundation of China (No. 81630096).

Availability of data and materials

No datasets were generated or analysed during the current study.

Declarations

Competing interests

The authors declare no competing interests.

Received: 26 January 2024 Accepted: 18 August 2024

References

1. Li J, Cao F, Yin HL, Huang ZJ, Lin ZT, Mao N, Sun B, Wang G. Ferroptosis: past, present and future. Cell Death Dis. 2020;11(2):88.
2. Xie Y, Hou W, Song X, Yu Y, Huang J, Sun X, Kang R, Tang D. Ferroptosis: process and function. Cell Death Differ. 2016;23(3):369–79.
3. Comporti M, Maellaro E, Del Bello B, Casini AF. Glutathione depletion: its effects on other antioxidant systems and hepatocellular damage. Xenobiotica. 1991;21(8):1067–76.
4. Chen Y, Dong H, Thompson DC, Shertzer HG, Nebert DW, Vasiliou V. Glutathione defense mechanism in liver injury: insights from animal models. Food Chem Toxicol. 2013;60:38–44.
5. Sun Y, Xia X, Basnet D, Zheng JC, Huang J, Liu J. Mechanisms of ferroptosis and emerging links to the pathology of neurodegenerative diseases. Front Aging Neurosci. 2022;14:904152.
6. Jakaria M, Belaidi AA, Bush AI, Ayton S. Ferroptosis as a mechanism of neurodegeneration in Alzheimer's disease. J Neurochem. 2021;159(5):804–25.
7. Du L, Wu Y, Fan Z, Li Y, Guo X, Fang Z, Zhang X. The role of ferroptosis in nervous system disorders. J Integr Neurosci. 2023;22(1):19.
8. Yang WS, Stockwell BR. Ferroptosis: death by lipid peroxidation. Trends Cell Biol. 2016;26(3):165–76.
9. Liang D, Minikes AM, Jiang X. Ferroptosis at the intersection of lipid metabolism and cellular signaling. Mol Cell. 2022;82(12):2215–27.
10. Dixon SJ, Lemberg KM, Lamprecht MR, Skouta R, Zaitsev EM, Gleason CE, Patel DN, Bauer AJ, Cantley AM, Yang WS, et al. Ferroptosis: an iron-dependent form of nonapoptotic cell death. Cell. 2012;149(5):1060–72.
11. Jollow DJ, Thorgeirsson SS, Potter WZ, Hashimoto M, Mitchell JR. Acetaminophen-induced hepatic necrosis. VI. Metabolic disposition of toxic and nontoxic doses of acetaminophen. Pharmacology. 1974;12(4–5):251–71.
12. Tirmenstein MA, Nelson SD. Acetaminophen-induced oxidation of protein thiols. Contribution of impaired thiol-metabolizing enzymes and the breakdown of adenine nucleotides. J Biol Chem. 1990;265(6):3059–65.
13. Ali Khan H, Mutus B. Protein disulfide isomerase a multifunctional protein with multiple physiological roles. Front Chem. 2014;2:70.
14. Wilkinson B, Gilbert HF. Protein disulfide isomerase. Biochim Biophys Acta. 2004;1699(1–2):35–44.
15. Galligan JJ, Petersen DR. The human protein disulfide isomerase gene family. Hum Genomics. 2012;6(1):6.
16. Turano C, Coppari S, Altieri F, Ferraro A. Proteins of the PDI family: unpredicted non-ER locations and functions. J Cell Physiol. 2002;193(2):154–63.
17. Xiong B, Jha V, Min JK, Cho J. Protein disulfide isomerase in cardiovascular disease. Exp Mol Med. 2020;52(3):390–9.
18. Wang L, Wang X, Wang CC. Protein disulfide-isomerase, a folding catalyst and a redox-regulated chaperone. Free Radic Biol Med. 2015;83:305–13.
19. Grek C, Townsend DM. Protein disulfide isomerase superfamily in disease and the regulation of apoptosis. Endoplasmic Reticulum Stress Dis. 2014;1(1):4–17.
20. Araki K, Iemura S, Kamiya Y, Ron D, Kato K, Natsume T, Nagata K. Ero1-α and PDIs constitute a hierarchical electron transfer network of endoplasmic reticulum oxidoreductases. J Cell Biol. 2013;202(6):861–74.
21. Araki K, Nagata K. Functional in vitro analysis of the ERO1 protein and protein-disulfide isomerase pathway. J Biol Chem. 2011;286(37):32705–12.
22. Hou MJ, Wang P, Zhu BT. Biochemical mechanism of erastin-induced ferroptotic cell death in neuronal cells. Acta Biochim Biophys Sin (Shanghai). 2023;55(5):853–65.
23. Wang H, Wang P, Zhu BT. Mechanism of erastin-induced ferroptosis in MDA-MB-231 human breast cancer cells: evidence for a critical role of protein disulfide isomerase. Mol Cell Biol. 2022;42(6):e0052221.
24. Okada K, Fukui M, Zhu BT. Protein disulfide isomerase mediates glutathione depletion-induced cytotoxicity. Biochem Biophys Res Commun. 2016;477(3):495–502.
25. Nagpal L, Haque MM, Saha A, Mukherjee N, Ghosh A, Ranu BC, Stuehr DJ, Panda K. Mechanism of inducible nitric-oxide synthase dimerization inhibition by novel pyrimidine imidazoles. J Biol Chem. 2013;288(27):19685–97.
26. Musial A, Eissa NT. Inducible nitric-oxide synthase is regulated by the proteasome degradation pathway. J Biol Chem. 2001;276(26):24268–73.
27. Mizunaga T, Katakura Y, Miura T, Maruyama Y. Purification and characterization of yeast protein disulfide isomerase. J Biochem. 1990;108(5):846–51.
28. Ali D, Abbady A-Q, Kweider M, Soukkarieh C. Cloning, expression, purification and characterization of Leishmania tropica PDI-2 protein. Open Life Sci. 2016;11(1):166–76.
29. Gaschler MM, Stockwell BR. Lipid peroxidation in cell death. Biochem Biophys Res Commun. 2017;482(3):419–25.
30. Zoupa E, Pitsikas N. The Nitric Oxide (NO) Donor Sodium Nitroprusside (SNP) and its potential for the schizophrenia therapy: lights and shadows. Molecules. 2021;26(11):3196.
31. Goldstein S, Russo A, Samuni A. Reactions of PTIO and carboxy-PTIO with *NO, *NO2, and O2-*. J Biol Chem. 2003;278(51):50949–55.
32. Rosselet A, Feihl F, Markert M, Gnaegi A, Perret C, Liaudet L. Selective iNOS inhibition is superior to norepinephrine in the treatment of rat endotoxic shock. Am J Respir Crit Care Med. 1998;157(1):162–70.
33. Seker U, Nergiz Y, Aktas A, Akkus M, Ozmen MF, Uyar E, Soker S. Trolox is more successful than allopurinol to reduce degenerative effects of testicular ischemia/reperfusion injury in rats. J Pediatr Urol. 2020;16(4):465.e461-465.e468.
34. Zhitkovich A. N-Acetylcysteine: antioxidant, aldehyde scavenger, and more. Chem Res Toxicol. 2019;32(7):1318–9.
35. Halasi M, Wang M, Chavan TS, Gaponenko V, Hay N, Gartel AL. ROS inhibitor N-acetyl-L-cysteine antagonizes the activity of proteasome inhibitors. Biochem J. 2013;454(2):201–8.
36. Dangol S, Chen Y, Hwang BK, Jwa NS. Iron- and reactive oxygen species-dependent ferroptotic cell death in rice-magnaporthe oryzae interactions. Plant Cell. 2019;31(1):189–209.
37. Fujita I, Nobunaga M, Seki T, Kurauchi Y, Hisatsune A, Katsuki H. Cystamine-mediated inhibition of protein disulfide isomerase triggers aggregation of misfolded orexin-A in the Golgi apparatus and prevents extracellular secretion of orexin-A. Biochem Biophys Res Commun. 2017;489(2):164–70.

38. Hoffstrom BG, Kaplan A, Letso R, Schmid RS, Turmel GJ, Lo DC, Stockwell BR. Inhibitors of protein disulfide isomerase suppress apoptosis induced by misfolded proteins. Nat Chem Biol. 2010;6(12):900–6.
39. Choi HJ, Lee AJ, Kang KS, Song JH, Zhu BT. 4-hydroxyestrone, an endogenous estrogen metabolite, can strongly protect neuronal cells against oxidative damage. Sci Rep. 2020;10(1):7283.
40. Mallis RJ, Thomas JA. Effect of S-nitrosothiols on cellular glutathione and reactive protein sulfhydryls. Arch Biochem Biophys. 2000;383(1):60–9.
41. Matsusaki M, Okuda A, Matsuo K, Gekko K, Masuda T, Naruo Y, Hirose A, Kono K, Tsuchi Y, Urade R. Regulation of plant ER oxidoreductin 1 (ERO1) activity for efficient oxidative protein folding. J Biol Chem. 2019;294(49):18820–35.
42. Blais JD, Chin KT, Zito E, Zhang Y, Heldman N, Harding HP, Fass D, Thorpe C, Ron D. A small molecule inhibitor of endoplasmic reticulum oxidation 1 (ERO1) with selectively reversible thiol reactivity. J Biol Chem. 2010;285(27):20993–1003.
43. Yamada N, Karasawa T, Kimura H, Watanabe S, Komada T, Kamata R, Sampilvanjil A, Ito J, Nakagawa K, Kuwata H, et al. Ferroptosis driven by radical oxidation of n-6 polyunsaturated fatty acids mediates acetaminophen-induced acute liver failure. Cell Death Dis. 2020;11(2):144.
44. Liao J, Lu Q, Li Z, Li J, Zhao Q, Li J. Acetaminophen-induced liver injury: molecular mechanism and treatments from natural products. Front Pharmacol. 2023;14:1122632.
45. Jaeschke H, Adelusi OB, Akakpo JY, Nguyen NT, Sanchez-Guerrero G, Umbaugh DS, Ding WX, Ramachandran A. Recommendations for the use of the acetaminophen hepatotoxicity model for mechanistic studies and how to avoid common pitfalls. Acta Pharm Sin B. 2021;11(12):3740–55.
46. Glinghammar B, Rafter I, Lindström AK, Hedberg JJ, Andersson HB, Lindblom P, Berg AL, Cotgreave I. Detection of the mitochondrial and catalytically active alanine aminotransferase in human tissues and plasma. Int J Mol Med. 2009;23(5):621–31.
47. Desilva MG, Lu J, Donadel G, Modi WS, Xie H, Notkins AL, Lan MS. Characterization and chromosomal localization of a new protein disulfide isomerase, PDIp, highly expressed in human pancreas. DNA Cell Biol. 1996;15(1):9–16.
48. Chichiarelli S, Altieri F, Paglia G, Rubini E, Minacori M, Eufemi M. ERp57/PDIA3: new insight. Cell Mol Biol Lett. 2022;27(1):12.
49. Marcus N, Shaffer D, Farrar P, Green M. Tissue distribution of three members of the murine protein disulfide isomerase (PDI) family. Biochim Biophys Acta. 1996;1309(3):253–60.
50. Ferrari DM, Söling HD. The protein disulphide-isomerase family: unravelling a string of folds. Biochem J. 1999;339((Pt 1)(Pt 1)):1–10.
51. van Lith M, Hartigan N, Hatch J, Benham AM. PDILT, a divergent testis-specific protein disulfide isomerase with a non-classical SXXC motif that engages in disulfide-dependent interactions in the endoplasmic reticulum. J Biol Chem. 2005;280(2):1376–83.
52. Andreu CI, Woehlbier U, Torres M, Hetz C. Protein disulfide isomerases in neurodegeneration: from disease mechanisms to biomedical applications. FEBS Lett. 2012;586(18):2826–34.
53. Castillo V, Oñate M, Woehlbier U, Rozas P, Andreu C, Medinas D, Valdés P, Osorio F, Mercado G, Vidal RL, et al. Functional role of the disulfide isomerase ERp57 in axonal regeneration. PLoS ONE. 2015;10(9):e0136620.
54. Conway ME, Harris M. S-nitrosylation of the thioredoxin-like domains of protein disulfide isomerase and its role in neurodegenerative conditions. Front Chem. 2015;3:27.
55. Di Risola D, Ricci D, Marrocco I, Giamogante F, Grieco M, Francioso A, Vasco-Vidal A, Mancini P, Colotti G, Mosca L, et al. ERp57 chaperon protein protects neuronal cells from Aβ-induced toxicity. J Neurochem. 2022;162(4):322–36.
56. Honjo Y, Ito H, Horibe T, Takahashi R, Kawakami K. Protein disulfide isomerase-immunopositive inclusions in patients with Alzheimer disease. Brain Res. 2010;1349:90–6.
57. Linden T, Doutheil J, Paschen W. Role of calcium in the activation of erp72 and heme oxygenase-1 expression on depletion of endoplasmic reticulum calcium stores in rat neuronal cell culture. Neurosci Lett. 1998;247(2–3):103–6.
58. Paschen W, Gissel C, Linden T, Doutheil J. Erp72 expression activated by transient cerebral ischemia or disturbance of neuronal endoplasmic reticulum calcium stores. Metab Brain Dis. 1998;13(1):55–68.
59. Altintas DM, Gallo S, Basilico C, Cerqua M, Bocedi A, Vitacolonna A, Botti O, Casanova E, Rancati I, Milanese C, et al. The PSI Domain of the MET Oncogene Encodes a Functional Disulfide Isomerase Essential for the Maturation of the Receptor Precursor. Int J Mol Sci. 2022;23(20):12427.

Publisher's Note